Available online at www.sciencedirect.com
SCIENCE DIRECT
Icarus 177 (2005) 32–62
ICARUS
www.elsevier.com/locate/icarus

Radar imaging of Saturn's rings

Philip D. Nicholson [a,*], Richard G. French [b], Donald B. Campbell [a], Jean-Luc Margot [a], Michael C. Nolan [c], Gregory J. Black [d], Heikki J. Salo [e]

[a] *Department of Astronomy, Cornell University, Ithaca, NY 14853, USA*
[b] *Department of Astronomy, Wellesley College, Wellesley, MA 02481, USA*
[c] *NAIC/Arecibo Observatory, HCO3, Box 53995, Arecibo, PR 00612, USA*
[d] *Department of Astronomy, University of Virginia, Charlottesville, VA 22901, USA*
[e] *University of Oulu, Astronomy Division, P.O. Box 3000, Oulu FIN-90014, Finland*

Received 24 June 2004; revised 22 February 2005

Available online 24 May 2005

Abstract

We present delay–Doppler images of Saturn's rings based on radar observations made at Arecibo Observatory between 1999 and 2003, at a wavelength of 12.6 cm and at ring opening angles of $20.1° \leqslant |B| \leqslant 26.7°$. The average radar cross-section of the A ring is ∼77% relative to that of the B ring, while a stringent upper limit of 3% is placed on the cross-section of the C ring and 9% on that of the Cassini Division. These results are consistent with those obtained by Ostro et al. [1982, Icarus 49, 367–381] from radar observations at $|B| = 21.4°$, but provide higher resolution maps of the rings' reflectivity profile. The average cross-section of the A and B rings, normalized by their projected unblocked area, is found to have decreased from 1.25 ± 0.31 to 0.74 ± 0.19 as the rings have opened up, while the circular polarization ratio has increased from 0.64 ± 0.06 to 0.77 ± 0.06. The steep decrease in cross-section is at variance with previous radar measurements [Ostro et al., 1980, Icarus 41, 381–388], and neither this nor the polarization variations are easily understood within the framework of either classical, many-particle-thick or monolayer ring models. One possible explanation involves vertical size segregation in the rings, whereby observations at larger elevation angles which see deeper into the rings preferentially see the larger particles concentrated near the rings' mid-plane. These larger particles may be less reflective and/or rougher and thus more depolarizing than the smaller ones. Images from all four years show a strong $m = 2$ azimuthal asymmetry in the reflectivity of the A ring, with an amplitude of ±20% and minima at longitudes of $67 \pm 4°$ and $247 \pm 4°$ from the sub-Earth point. We attribute the asymmetry to the presence of gravitational wakes in the A ring as invoked by Colombo et al. [1976, Nature 264, 344–345] to explain the similar asymmetry long seen at optical wavelengths. A simple radiative transfer model suggests that the enhancement of the azimuthal asymmetry in the radar images compared with that seen at optical wavelengths is due to the forward-scattering behavior of icy ring particles at decimeter wavelengths. A much weaker azimuthal asymmetry with a similar orientation may be present in the B ring.

1. Introduction

Our modern understanding of the physical nature of the particles which comprise the rings of Saturn dates to the early 1970s, when the first, unexpectedly strong radar echoes were obtained at a wavelength of 12.6 cm (Goldstein and Morris, 1973). Early delay–Doppler observations of Saturn's rings, made at Arecibo in 1976 by Ostro et al. (1982), demonstrated that (i) most if not all of the reflected power came from the A and B rings, (ii) the A ring's reflectivity is ∼90% of the B ring's, and (iii) the reflectivity of the C ring is probably ⩽10% that of the B ring. These observations, together with additional CW (continuous wave) radar experiments at 3.5 cm (using the 70 m Deep Space Network antenna at Goldstone, CA) and 12.6 cm (primarily at Arecibo) in the late 1970s (Goldstein et al., 1977; Ostro et al., 1980), demonstrated conclusively that typical ring particles must be decimeters in size or larger. The very

* Corresponding author.
E-mail address: nicholso@astro.cornell.edu (P.D. Nicholson).

0019-1035/$ – see front matter
doi:10.1016/j.icarus.2005.03.023

high normalized radar cross-section ($1.0 \leqslant \hat{\sigma}_T \leqslant 1.4$) coupled with the rings' very low microwave brightness temperature ($T_B \approx 10$ K; Berge and Muhleman, 1973) could plausibly be reconciled only by centimeter-to-meter-sized chunks of water ice, whose very low absorption coefficient at a physical temperature of ∼90 K leads to a correspondingly low microwave emissivity (Pollack et al., 1973; Pettengill and Hagfors, 1974; Pollack, 1975).

A long-standing puzzle in the study of Saturn's rings is the issue of the rings' thickness and vertical structure. Photometric observations made when the Earth crosses the ring plane yield effective global thicknesses of 1.0–1.5 km (Sicardy et al., 1982; Nicholson et al., 1996), but this residual edge-on brightness is now known to be dominated by the F ring (Nicholson et al., 1996; Poulet et al., 2000). A stellar occultation observed by the Voyager 2 photopolarimeter instrument provided an upper limit of 200 m on the local thickness in the vicinities of several sharp edges in the A, B, and C rings (Lane et al., 1982). Analysis of the bistatic scattering data from the Voyager 1 radio occultation experiment led to the conclusion that the C ring may be effectively a monolayer, while the meter-size particles in the A ring are confined to a layer approximately 3 particles thick (Zebker et al., 1985). Zebker and Tyler (1984) inferred a thickness of less than 10 m in the C ring and ∼50 m in the A ring.

These more-or-less direct observational limits are consistent with dynamical simulations which suggest that the scale height, $H = 10$–20 m (Goldreich and Tremaine, 1978; Cuzzi et al., 1979; Salo, 1995), and with ring thicknesses of 30 m or less inferred from density and bending wave damping lengths (Esposito et al., 1983b). On the other hand, most optical photometric models have assumed a classical, many-particle thick ring (e.g., Dones et al., 1993; Doyle et al., 1989; Cooke, 1991). Analyses of the rings' radar cross-section and polarization characteristics and their variation with opening angle provide an independent avenue to attack this problem (Cuzzi and Pollack, 1978; Ostro et al., 1980).

Cuzzi and Pollack (1978) and Cuzzi et al. (1980) used both radar and radio emission observations to develop physical models of the rings based on classical radiative transfer methods and a new model of scattering by large, irregular particles. They considered models with the particles in a monolayer, and distributed over a layer several particle diameters thick. Comparisons of these model predictions with variations of the rings' radar cross-section as a function of opening angle, B, indicated that only the many-particle-thick model was satisfactory, while the similarity of the radar cross-sections at 3.5 and 12.6 cm supported the idea of a broad size distribution extending from a few centimeters to several meters (Ostro et al., 1980; Ostro and Pettengill, 1984).

Definitive information on the particle size distribution was provided by the radio occultation experiment carried out at 3.5 and 13 cm by the Voyager 1 spacecraft in 1980 (Tyler et al., 1983). Inversion of the forward-scattering cross-sections of the A and C rings led to size distributions with upper cutoffs at ∼5 m, while the differential opacity data were consistent with power-law distributions in the 1 cm to 1 m range with indices of $q = 2.8$–3.4 (Marouf et al., 1983). Further attempts to constrain the rings' particle size distribution based on stellar occultation data at optical wavelengths have been made by Showalter and Nicholson (1990) and French and Nicholson (2000). The latter estimated minimum and maximum radii in the A and B rings of 30 cm and 20 m, with $q \approx 2.75$, but a somewhat steeper distribution in the C ring ($q \approx 3.1$) with particle radii in the 1 cm to 10 m range.

Other unanswered questions remain concerning the microstructure of the rings and the physical nature of the ring particles. One of the most intriguing is the origin of the so-called azimuthal asymmetry exhibited by the A ring at optical wavelengths. This quasi-sinusoidal variation in brightness with longitude has been observed photographically with ground-based telescopes (Camichel, 1958; Reitsema et al., 1976; Thompson et al., 1981), in images taken by the Pioneer 11 (Gehrels and Esposito, 1981) and Voyager spacecraft (Dones et al., 1993), and most recently in Hubble images (French et al., 2000). In all cases, the ring is fainter in the first and third quadrants as measured from the observer's position in the direction of orbital motion, reaching a minimum ∼20° in longitude prior to the particles reaching elongation (Lumme and Irvine, 1984), and brighter in the second and fourth quadrants. The effect is strongest in the middle A ring, where it can reach an amplitude of ±20% at intermediate ring opening angles ($B \simeq 12°$) and apparently rotates to maintain a fixed orientation with respect to the observer (Dones et al., 1993). Based on the available data, the asymmetry seems to be independent of both wavelength and solar phase angle, but decreases in amplitude at lower and higher values of B.

The most widely-accepted explanation of the azimuthal asymmetry involves gravitational 'wakes' generated spontaneously or by individual large ring particles, which are distorted by Keplerian shear into elongated structures trailing at angles of ∼70° from the radial direction (Colombo et al., 1976; Franklin and Colombo, 1978; Salo, 1995; Daisaka and Ida, 1999). Such wakes are indicative of incipient gravitational instability near the Roche limit, and are expected to have characteristic wavelengths of ∼75 m in the A ring (Salo, 1992a; Salo et al., 2004). They are analogous to the stellar wakes in galactic disks first studied by Julian and Toomre (1966) and reviewed by Toomre and Kalnajs (1991). If this picture is indeed correct, then the asymmetry should be equally visible in radar images of the rings. The only previous delay–Doppler observations of the rings, made at Arecibo in 1976 at $B = -21.4°$ (Ostro et al., 1982) had insufficient signal-to-noise ratio to resolve the question of azimuthal variations, though there is a hint of such an asymmetry in the data.

Since 1978, Saturn has been too far south for observations at Arecibo and no additional radar observations

of the rings have been reported. Only in late 1998 did the planet return to a declination where the tracking time at Arecibo exceeded the round-trip light travel time of ∼135 min. In October 1999 we commenced a program of annual delay–Doppler imaging of Saturn using the recently-upgraded Arecibo S-band ($\nu = 2380$ MHz, $\lambda = 12.6$ cm) planetary radar system. Our primary goals were to search for the azimuthal asymmetry in the A ring, as well as to examine the dependence of the rings' cross-section and circular polarization ratio on opening angle. A third goal was to investigate the mysterious low Doppler excess (LDE) seen in radar observations of the rings in the early 1970s, an excess of power observed at low Doppler frequencies and $|B| \geqslant 24°$ at both 3.5 and 12.6 cm by Goldstein et al. (1977). The LDE did not appear at $B = -21.4°$ or at lower inclinations, and no satisfactory explanation for it has been advanced.

In this paper we report on our first four years of observations, during which the opening angle, $|B|$, has increased from 20.1° to a (near maximum) value of 26.7°. Delay–Doppler images are presented for each year, along with estimated radar cross-sections and polarization ratios for the A and B rings. The azimuthal asymmetry is clearly seen in all years, with an unexpectedly large amplitude. No evidence is found of the LDE, and no echo was detected from the C ring. In Sections 2 and 3 we describe our observations and the data analysis necessary to produce calibrated delay–Doppler images, respectively. The resulting ring cross-sections and radial reflectivity profiles are presented in Section 4, and our results are discussed in the context of previous work. In Section 5 we obtain quantitative estimates of the amplitude and phase of the azimuthal asymmetry. Section 6 presents a radiative transfer model for the A ring asymmetry, based on the Monte Carlo light scattering model of Salo et al. (2004). Our conclusions are summarized in Section 7.

2. Observations

The main limitation to radar observations of Saturn at Arecibo was alluded to above: the minimum round-trip light travel time to Saturn at opposition is ∼134 min, whereas the maximum available tracking time on a target at the optimal declination near Arecibo's latitude of +18.2° is only 166 min, dictated by the telescope's maximum zenith angle of 19.7°. Only for declinations north of +8.5° does the tracking time exceed the two-way light time. This limits observations in the current saturnian year to between October 1998 and February 2008. Even in optimal years, the available integration time 'on target' is at most ∼32 min per day. For our observations the actual receive time per day ranged from 22 to 31 min (see Table 1 for the relevant observational parameters).

The remaining limitations are imposed by the geometry of the ring system itself. Fig. 1 illustrates the mapping of delay–Doppler cells onto the approaching ansa of the rings, for $|B| = 25.8°$ (corresponding to December 2001). Horizontal lines are lines of constant delay, while the curving lines are contours of constant Doppler shift, as determined by the Keplerian velocity profile across the rings. The situation on the opposite ansa is a mirror image of Fig. 1, but with negative Doppler shifts; there is no east–west ambiguity analogous to the north–south ambiguity which afflicts delay–Doppler imaging of rigidly-rotating planets and asteroids. Note that the maximum Doppler shift of ∼325 kHz occurs at the ansa, at the innermost edge of the C ring, while zero Doppler corresponds both to the subradar longitude on the rings and to its counterpart 180° away. An important feature illustrated in Fig. 1, and one which severely affects the interpretation of delay–Doppler images of the rings, is the degeneracy of delay and Doppler cells which occurs ∼35° on either side of each ansa. At these four symmetrically-placed locations the Doppler contours are locally parallel to constant-delay lines and a substantial quasi-radial slice of the rings can contribute to the same delay–Doppler cell. Not only does this degeneracy lead to the four prominent bright spots seen in all our images (cf. Fig. 2), but it prevents a straightforward inversion of the delay–Doppler maps into maps of the rings in physical coordinates (either x, y or r, θ). Away from these four regions, the delay and Doppler contours are reasonably orthogonal and permit an unambiguous mapping of the rings' radar reflectivity in radius and longitude.

A final complication arises from the 'overspread' character of the radar echo from the rings. A typical slowly-rotating terrestrial radar target (e.g., Mercury or Venus) might have a delay 'depth' of $\Delta\tau = 2R_{\rm planet}/c \simeq 20$–40 ms, while the Doppler width of its radar echo at 2380 MHz is of order $\Delta\nu = 8\pi R_{\rm planet}\nu_0/Pc \simeq 150$ Hz for a synodic rotation period of $P = 100$ days. As long as the product $\Delta\tau\Delta\nu$ is not much greater than unity, the target may be mapped simultaneously in delay (i.e., range from the observer) and Doppler shift using coherent techniques involving pseudo-random phase coding of the continuous-wave (CW) transmitted signal (Evans and Hagfors, 1968; Ostro, 1993). But if this non-aliasing condition is violated, the target is referred to as 'overspread' and such techniques fail.

Saturn's rings are overspread with a vengeance: the delay depth is $\Delta\tau = 4R_{\rm outer}\cos B/c \simeq 1.72$ s at $|B| = 20°$, where $R_{\rm outer} = 1.37 \times 10^5$ km is the outer radius of the A ring, while the Doppler width at the inner edge of the C ring is $\Delta\nu = 4\Omega R_{\rm inner}\nu_0 \cos B/c = 676$ kHz, so that $\Delta\tau\Delta\nu \simeq 1.2 \times 10^6$. In practical terms, this means that successive short transmitted pulses of CW radiation return spread over almost 700 kHz in frequency and must be separated by at least 1.8 s to avoid range aliasing problems.

In such a situation, i.e., when $\Delta\tau\Delta\nu \gg 1$, a simpler, incoherent technique can be used (Ostro et al., 1982; Campbell and Hudson, 2002). A delay–Doppler image of the returned power is generated from each individual transmitted pulse and then a weighted average is constructed by summing all the images so obtained. The resolution in time delay is lim-

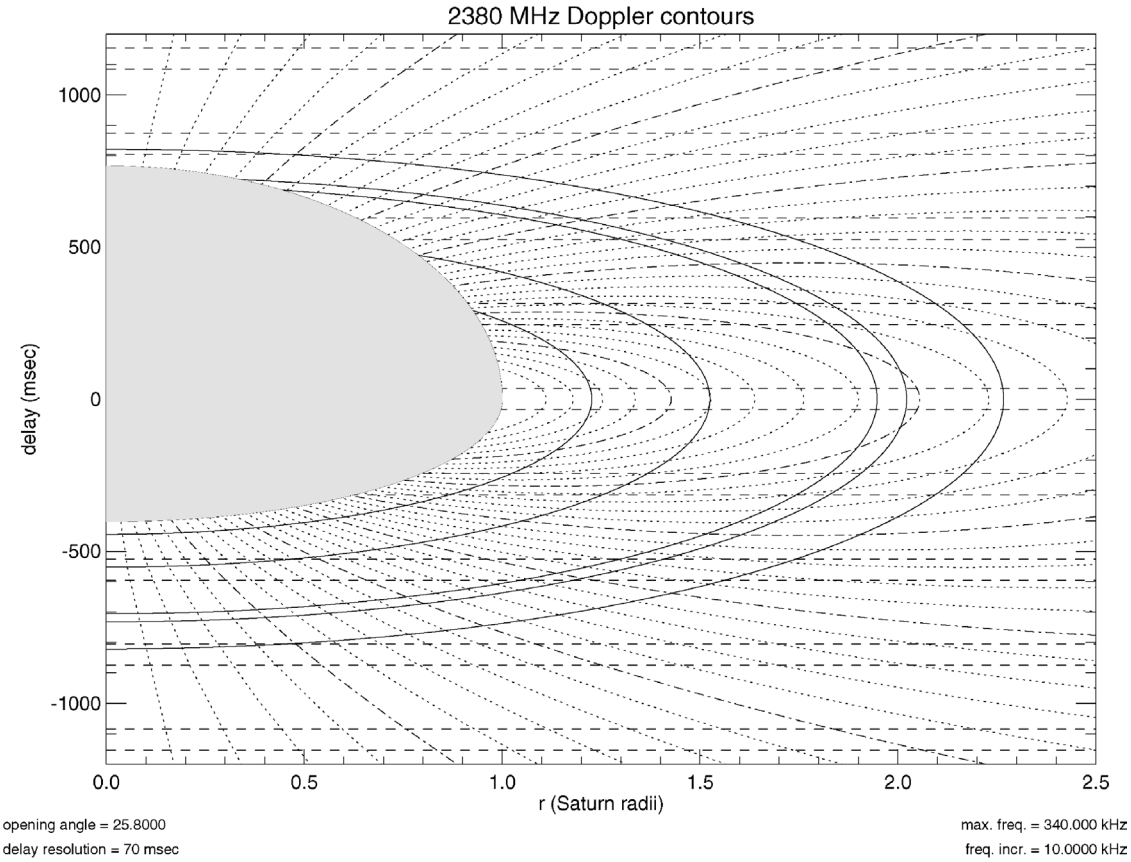

Fig. 1. Contours of constant time delay and Doppler shift at S-band across the eastern or approaching side of Saturn's rings for December 2001. Dashed lines indicate every fourth 70 ms range box, while dotted and dot-dashed lines indicate Doppler contours at 10 and 50 kHz intervals. The planet and its shadow on the rings are blanked out. The Doppler shifts change sign on the western side of the rings, so there is no east–west ambiguity analogous to the 'north–south ambiguity' which afflicts solid-body radar imaging, but parallel delay and Doppler bins result in a local radial degeneracy near $\pm 35^\circ$ from the ansa, resulting in the four bright spots seen in Fig. 2.

ited by the pulse length and in the Doppler dimension by its inverse.

2.1. Transmitter operations

To avoid the overspread difficulties, and make efficient use of the limited observing time available each day, our observations employed a frequency stepped (or 'hopping') technique (cf. Ostro et al., 1982) with a CW pulse length of 70 ms, increasing the transmitter frequency by 800 kHz between successive pulses. In most years, 21 such 'hops' were used, driving the transmitter over a range of 16 MHz centered on a frequency of 2380 MHz. After pausing briefly at the highest frequency, the cycle was repeated with a pulse repetition period (PRP) of 2.03 s, comfortably longer than the delay depth of the rings and leaving $\sim$0.3 s in each cycle for background measurements.

The transmitter frequency was also continuously adjusted to compensate for the varying 2-way Doppler shift between Arecibo and Saturn, so that a hypothetical echo from the planet's center of mass would return exactly at 2380 MHz modulo the 800 kHz hop offsets. The pulses were transmitted with a left circular polarization (IEEE definition).

Over the four years of observations several variations on the above protocol were used in an attempt to maximize efficiency and balance better delay resolution against a higher transmitter duty cycle. Details are given in Table 1. The 70 ms pulse length, 21 hops, and 2.03 s PRP adopted in 2001 and 2003 provide a range resolution of 10,500 km and an effective duty cycle of 69% for a receiver bandwidth of 16 MHz. For comparison, Ostro et al. (1982) used a similar strategy but with a pulse length of 400 ms, 8 hops and a PRP of 3.2 s, with a corresponding range resolution of 60,000 km. Their maps were made at an opening angle of 21.4°. It is the improvement in the telescope's gain as a result of the Gregorian upgrade, coupled with a doubling of transmitter power and the advent of wider-bandwidth digital sampling systems, which has permitted us to improve significantly on the earlier results.

The only problem encountered with this mode of observations, which were carried out with the transmitter and telescope under full computer control, was a series of unpredictable transmitter anomalies which led to automatic shutdowns and subsequent loss of data. These were apparently associated with the unusually large variations in klystron driving frequency. These dropouts limited the data obtained

Table 1
Summary of observations

	1999	2000	2001	2003
UT dates	October 24–November 1	November 19–23	December 17–22	January 3–8
Ring opening angle, B	−20.1°	−23.5°	−25.8°	−26.7°
Two-way light time, τ_{RT} (min)	137	135	135	135
Transmit parameters:				
Average transmitted power, P (kW)	450	750	800	800
Pulse length (ms)	50[a] or 100	70	70	70
Frequency steps, N_{hops}	16	25	25 or 21[b]	21 or 19[c]
Hop increment (kHz)	800	800	800	800 or 700[c]
Pulse repetition period, PRP (s)	2.20	2.03	2.03	2.03
Receive parameters:				
CBR bandwidth (MHz)	13[a] or 10	10	10	10
PFS bandwidth (MHz)	–	20	20 or 16[b]	16
Available time per day (min)	22	29	31	30
Antenna gain[d] (K/Jy)	6.6	5.8	9.2	8.9
OC T_{sys}[d] (K)	31.9	27.2	26.5	28.4
SC T_{sys}[d] (K)	29.8	26.4	25.4	23.6
Total OC receive time (min)	103	87	67	58
Total SC receive time (min)	103	91	65	47

[a] October 24.
[b] December 19 and 22.
[c] January 7 and 8.
[d] At an average zenith angle of 16.3°.

on one of five nights in 2000, on two of four nights in 2001, and on three of six nights in 2003. Attempts to circumvent the problem by reducing either the number of hops or the total hop bandwidth were unsuccessful. Although no such problems were encountered in October 1999, one of the two 500 kW S-band klystrons was out of service for maintenance and retuning, reducing the total transmitted power by 50%.

2.2. Signal recording

The return signal was recorded in both the Opposite Circular and Same Circular polarizations (henceforth referred to as OC and SC, respectively). After passing through intermediate frequency stages at 750 and 260 MHz, the baseband signal with its bandwidth of ∼16.8 MHz was low-pass filtered to avoid aliasing, amplified, and sampled using two independent receivers: the Caltech Baseband Pulsar Receiver (CBR) operating at 10 MHz, with two channels (OC and SC) and 2-bit sampling and a newly built Portable Fast Sampler (PFS) operating at up to 20 MHz with 1 channel (OC only) and at 2 or 4 bits per sample. The exact sampling frequencies were readjusted slightly on each night to allow for the changing two-way light time and so as to maintain a fixed number of samples per returning PRP (2.03×10^7 for the CBR and 3.248×10^7 for the PFS operating at 16 MHz). Data were recorded on DLT tapes (CBR) and hard disk (PFS), with typical volumes of 10 and 16 Gbyte per night, respectively.

Table 1 summarizes our observations in all four years, including ring opening angle, B, and two-way light time, transmitter setup (average power, pulse length, number of frequency hops, and PRP time) and receive parameters (bandwidth, receive time per day and the total non-redundant integration time in each polarization for each observing run). Between the 2000 and 2001 runs, the telescope's primary reflector surface was reset, resulting in a substantial improvement in telescope gain for the last two years. This more than offset the shorter total integration time achieved in these years, and the 2001 observations yielded the highest signal-to-noise ratio images to date.

In October 1999, observations of the rings were made on five alternate days, interleaved with observations of Titan. No significant problems were encountered with either transmission or reception. Sixteen frequency hops were used, with a PRP of 2.20 s. Data were taken with the CBR running at 13 MHz on October 24 and on subsequent nights at 10 MHz; the PFS was still under development and used only for tests. On the first night a pulse length of 50 ms was used, but with a resulting transmitter duty cycle of only 36%. On subsequent nights this was increased to 100 ms and the CBR sampling rate reduced to 10 MHz (=12 hops) to avoid potential aliasing problems; the duty cycle was 55%.

In November 2000 we observed for five consecutive nights with a uniform setup of 25 frequency hops, a PRP of 2.03 s and both klystrons in operation. Both the PFS and CBR were used for data recording, the latter sampling at 10 MHz and the former at its maximum design rate of 20 MHz. Problems with the PFS resulted in a loss of useful data on November 19, 21, and 23, while a transmitter failure on November 19 limited useful observing time to 9 min. The CBR also failed on November 23. Overall, three good nights of data were obtained with the CBR and two with the PFS.

In 2001 we observed Saturn for four nights over December 17–22, with the nights of December 20 and 21 devoted to Titan. The initial transmitter setup was as in the previous

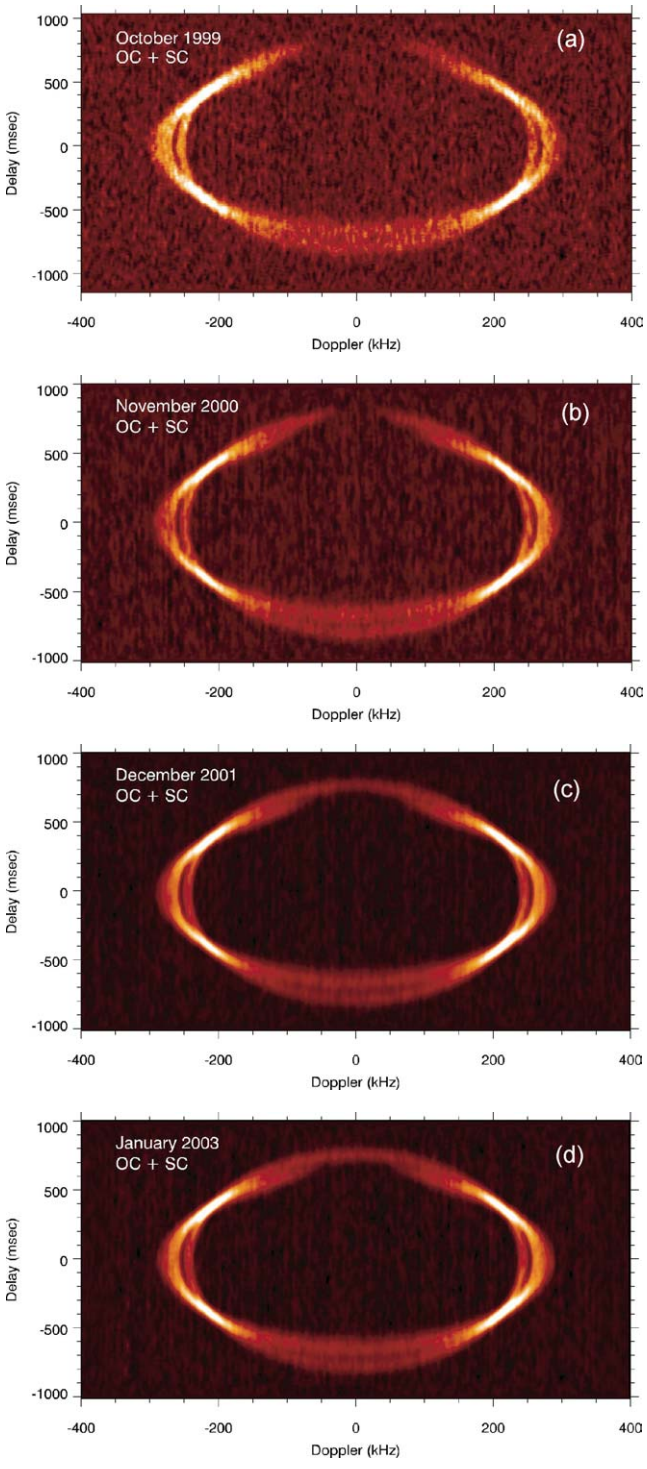

Fig. 2. Delay–Doppler images constructed from data obtained in (a) October 1999, (b) November 2000, (c) December 2001, and (d) January 2003. Both OC and SC polarizations were combined to maximize the signal to noise ratio. Note the four bright regions in each image where the delay and Doppler cells are parallel and where the A and B rings appear to cross over one another.

year, but persistent problems with ghost images in the PFS data and a transmitter shutdown on December 18 led us to reduce the number of frequency hops to 21 and the PFS sampling rate to 16 MHz for the last two nights. Unfortunately both the transmitter and the CBR failed on December 19, and good data were obtained from both receivers only on December 22. Good CBR data were also obtained on December 17. Despite these woes, the overall SNR of the images obtained from this run is the highest of all four years, due to the improved telescope gain.

In 2003, observations were attempted on January 3–8, using the same transmitter setup as finally adopted in 2001 (i.e., 21 frequency hops, a PRP of 2.03 s, and recording at 10 MHz (CBR) and 16 MHz (PFS)). Useful observations of Saturn on January 4–6 were prevented by background synchrotron radiation from the nearby Crab Nebula (M1). Of the remaining three nights, 12 min were lost to a transmitter failure on January 3 and almost 20 min were similarly lost on January 8. On January 7 a full 30 min of data was successfully recorded with both receivers.

3. Delay–Doppler images

3.1. Data processing

Successive 0.5 ms segments of data were Fourier transformed to produce power spectra at a resolution of $\delta\nu = 2$ kHz, which were incoherently co-added over a period of $\delta\tau = 10$ ms to produce 203 spectra per PRP, and saved in binary files of either $N_{\rm cyc} = 30$ PRPs for the CBR data or 25, 50, or 100 PRPs for the PFS data. In subsequent processing ('dehopping') we time-shifted each successive spectral interval of 800 kHz (400 points) by 7 delay bins (70 ms), so as to align the echoes in time across all frequencies, and then summed the $N_{\rm cyc}$ PRPs within each file of data. Each summed spectrum, $S(\nu,\tau)$, was then corrected for and normalized by the average background noise spectrum, $B(\nu)$, measured during the intervals of ∼0.3 s between successive ring echoes:

$$s(\nu,\tau) = S(\nu,\tau)/B(\nu) - 1, \tag{1}$$

where $-8 \leqslant \nu \leqslant 8$ MHz and $-1.015 \leqslant \tau \leqslant 1.015$ s. Next, the $N_{\rm hops} = 20$ separate frequency hops[1] within the 16 MHz PFS bandwidth (or $N_{\rm hops} = 12$ within 10 MHz bandwidth of the CBR) were stacked and averaged to produce a single 400×203 pixel delay–Doppler image from each file of data and for each polarization:

$$I(\nu,\tau) = \frac{(N_{\rm cyc}N_{\rm hops}\delta\tau\delta\nu N_{\rm back})^{1/2}}{N_{\rm hops}(N_{\rm back}+1)^{1/2}} \sum_{1}^{N_{\rm hops}} s(\nu,\tau), \tag{2}$$

where $-400 \leqslant \nu \leqslant 400$ kHz and $-1.015 \leqslant \tau \leqslant 1.015$ s. With this normalization, the RMS background noise in each image is unity (Ostro et al., 1992). $N_{\rm back}$ is the number of spectra coadded to estimate $B(\nu)$, typically 14 or 28.

[1] For simplicity, we quote numerical values for the 2001 and 2003 data.

Table 2
Daily log of observations

Date (UT)	P (kW)	CBR[a] $N_{\rm hops}$	CBR[a] $N_{\rm cyc}$	CBR[a] $N_{\rm files}$	PFS[b] $N_{\rm hops}$	PFS[b] $N_{\rm cyc}$	PFS[b] $N_{\rm files}$
1999 October 24	470	16	30	19	–	–	–
1999 October 26	480	12	30	18	–	–	–
1999 October 28	450	12	30	19	–	–	–
1999 October 30	440	12	30	18	–	–	–
1999 November 1	445	12	30	20	–	–	–
2000 November 19	850	12	30	9	–	–	–
2000 November 20	890	12	30	29	24	25	31
2000 November 21	860	12	30	23	–	–	–
2000 November 22	860	12	30	29	24	25	35
2001 December 17	900	12	30	30	–	–	–
2001 December 18	820	12	30	4	–	–	–
2001 December 19	880	–	–	–	20	50	1
2001 December 22	830	12	30	30	20	50	18
2003 January 3	890	12	30	17	20	100	5
2003 January 7	750	12	30	29	18	100	9
2003 January 8	760	–	–	–	18	100	3

Note. $N_{\rm hops}$ is the number of frequency hops within the receiver bandwidth, $N_{\rm cyc}$ is the number of PRPs summed in each file of data, and $N_{\rm files}$ is the number of files of data included from each night in the final images.
[a] OC and SC polarizations.
[b] OC polarization only.

Up to 30 such 'snapshots' of CBR data were obtained on each night (at 60.9 s per file), and between 9 and 35 snapshots of PFS data (at 50.75, 101.5, or 203.0 s per file). Table 2 provides a daily log of observations, including the average transmitter power and the number of files of 'good' data obtained with each receiver on each night, along with the corresponding values of $N_{\rm hops}$ and $N_{\rm cyc}$. Images exhibiting 'ghosts' or other obvious artifacts are excluded from Table 2, and from the co-added images used in our subsequent analysis.

After visual inspection of the individual images, the OC and SC images were separately weighted and co-added to produce a pair of master OC and SC images for each observing run. The weighting scheme, based again on Ostro et al. (1992), utilized existing calibration data for the telescope gain (g) and system temperature ($T_{\rm sys}$) as functions of zenith angle and azimuth (Phil Perillat, private communication). These calibrations were revised and improved after the primary antenna surface was reset in 2001. In terms of the single-snapshot images for the kth night, I_{jk}, the co-added image for one night is given by:

$$I_k(\nu,\tau) = \frac{1}{W_k}\sum_{j=1}^{N_{\rm files}} w_{jk} I_{jk}(\nu,\tau), \tag{3}$$

where the individual snapshot weights are

$$w_{jk} = \frac{g_t g_r P_k}{T_{\rm sys}} (N_{\rm cyc} N_{\rm hops})^{1/2} \tag{4}$$

and the total nightly weight is

$$W_k = \left(\sum_{j=1}^{N_{\rm files}} w_{jk}^2\right)^{1/2}. \tag{5}$$

The transmit and receive gains, g_t and g_r as well as $T_{\rm sys}$ were evaluated for each snapshot, due to the rapid variation in these quantities close to the telescope's zenith limit, but the average radiated power, P_k was recorded only once for each night (see Table 2).

Combining data from several nights and from both PFS and CBR receivers for the OC polarization we obtained our final images for each run:

$$I(\nu,\tau) = \frac{1}{W}\sum_k W_k I_k(\nu,\tau), \tag{6}$$

where the associated total weight is given by

$$W = \left(\sum_k W_k^2\right)^{1/2} = \left(\sum_k \sum_j w_{jk}^2\right)^{1/2}. \tag{7}$$

Five such images were created for each run: separate PFS (OC) and CBR (OC and SC) images, a combined OC image,[2] and an unpolarized image

$$I_{\rm tot}(\nu,\tau) = \frac{W_{\rm OC} I_{\rm OC} + W_{\rm SC} I_{\rm SC}}{(W_{\rm OC}^2 + W_{\rm SC}^2)^{1/2}}. \tag{8}$$

With the normalization of the individual snapshots, I_{jk}, given in Eqs. (1) and (2), the RMS noise level is unity (Ostro et al., 1992), and the signal from the rings is expressed as an SNR per pixel ($\delta\tau \times \delta\nu$). The weighting scheme preserves this aspect of the images. If, for example, all individual weights w_{jk} were equal then we have $W = N_{\rm snap}^{1/2} w$ where $N_{\rm snap}$ is the total number of snapshots combined and

$$\begin{aligned} I(\nu,\tau) &= N_{\rm snap}^{-1/2} w^{-1} \sum_k \sum_j w I_{jk}(\nu,\tau) \\ &= N_{\rm snap}^{1/2} \langle I_{jk} \rangle. \end{aligned} \tag{9}$$

The combined image is increased in SNR by a factor of $N_{\rm snap}^{1/2}$, as expected. Note also that the absolute value of the weights cancels out in the final expression for I, but is preserved in W to be used in the absolute calibration below.

As a check on the analysis, the mean and RMS noise levels in the final images were evaluated in two regions: one interior to the rings and one outside them. In all cases, the RMS noise was between 0.99 and 1.01, while the mean 'sky' signal was $\leqslant 0.02$. Table 3 lists the combined OC and SC weights, $W_{\rm OC}$, and $W_{\rm SC}$, for each run. These weights, while arbitrary in absolute value, provide a useful way to compare the quality and quantity of data obtained on each night and from run to run. The relatively low weights for the 1999 data reflect the lower transmitted power and shorter receive time per day, as well as the smaller number of hops per cycle for the CBR data. (Note that the SC and OC weights are not identical, even when only CBR data are used, due to slight variations in $T_{\rm sys}$ with polarization and the occasional bad snapshot excluded from the analysis.)

[2] In forming the combined OC image, we used either the PFS or CBR data for each night, based on which had the larger weight W_k. In most cases, the PFS data were used.

Table 3
Image weights[a]

	1999	2000	2001	2003
W_{OC}–CBR	0.981	1.851	3.849	2.862
W_{SC}–CBR	1.084	1.951	4.039	3.447
W_{OC}–PFS	–	2.096	3.418	3.916
W_{OC}-combined	0.981	2.362	4.491	3.916
W_{T}-combined	1.462	3.063	6.041	5.217

[a] In units of 10^5.

3.2. Ring images

The combined OC + SC image from each of our four observing runs is shown in Fig. 2. As no appreciable difference between the OC, SC and combined images is discernible to the eye, we do not show the individual SC and OC images. Time delay increases from bottom to top in each panel, and Doppler frequency increases from left to right. (Note that this puts the eastern or approaching side of the rings on the right side of the images and Saturn's south pole at the top, opposite the usual convention for optical images.) The far side of the rings was completely blocked by Saturn in 1999 and 2000, but the A ring became partially visible in 2001 (cf. Fig. 1) and completely so in 2003.

At our frequency resolution of 2 kHz, the effective radial resolution at the ring ansae ranges from 1100 km in the C ring to 2200 km in the A ring. In the delay dimension, the pixel size of $\delta\tau = 10$ ms corresponds to ∼1650 km in the ring plane, although the real radial resolution at the subradar point—as set by the transmitter pulse length of 70 ms—is ∼11,500 km.[3] With a width of 4500 km, the Cassini Division separating the A and B rings is clearly resolved at the ansae in all four years. It is also visible at the subradar point in 2000–2003.

Prominent in the image from each year are four bright features at $\nu = \pm 220$ kHz, $\tau = \pm 400$ ms and elongated parallel to the rings. These reflect the local delay–Doppler degeneracy illustrated in Fig. 1 and noted in Section 2. At these points a single delay–Doppler cell, or pixel, can extend across much of the A or B ring, collecting an unusually large fraction of the signal reflected from the rings. Towards the ring ansae from these points the B ring appears outside the A ring in the images, due to its greater Keplerian orbital velocity, whereas along the line of sight towards Saturn's center the B ring appears in its customary position interior to the A ring. The bright points can thus be thought of as the 'cross-over' points between A and B rings in delay–Doppler images, an impression reinforced by the best images. They fall at ∼35° either side of the ring ansae, or at longitudes with respect to the subradar point of ±55° and ±125°.

Noteworthy by its absence in the images is the inner or C ring, which is predicted to appear at a Doppler shift of 290–325 kHz at the ansae for $|B| = 26°$ (cf. Fig. 1). This is seen more clearly in Fig. 3, which displays smoothed Doppler profiles from December 2001 centered at zero delay and running across both ring ansae. The calculated maximum frequencies at the boundaries of the A, B, and C rings are shown as dotted lines; no signal is apparent from the C ring. The inner edge of the B ring at 290 kHz appears almost as sharp as the outer edge of the A ring at 237 kHz. This is consistent with the results of Ostro et al. (1982), who also failed to detect any signal from the C ring. Echoes from the equatorial limbs of Saturn would appear at $\nu = \pm 4\pi R_S \nu_0 \cos B / c P_S = \pm 141$ kHz in Fig. 3, but are also not seen.

We have searched for any evidence of the puzzling low Doppler excess (LDE) reported from radar spectra obtained in the early 1970s (Goldstein et al., 1977). This might have been expected to reappear in our data from 2001 and 2003, when $|B|$ once again exceeded 24°, but no signal unattributable to the A or B ring is evident in any of our images. Echoes at low Doppler shifts might be expected to arise either from near the subradar point on the planet itself or from ring material far outside the main rings. Our images show no evidence for any echo from the subradar point on Saturn, which would appear near $\nu = 0$ and $\tau = -2R_S/c = -402$ ms. This is illustrated best by the delay profiles through the planet, centered at zero Doppler shift, shown in Fig. 4. Only the expected signals from the front of the A and B rings and the back of the A ring are detected above the RMS noise level.

A possibility remains that the LDE might have its source in ring material well outside the main rings, such as the narrow G ring at $2.8R_S$ or the broad E ring at $3–8R_S$ (Cuzzi et al., 1984), although the latter is believed to be composed primarily of micron-sized ice dust. The peak Doppler shift from any such material would fall well within the ±400 kHz spectral range of our images ($\nu_{max} = 214$ kHz for the G ring and $\nu_{max} = 207$ kHz for the E ring), but the time delay with respect to Saturn's center of mass would fall at or beyond our window of ±1.015 s. As a result, any echo from the E ring would appear aliased in delay and superimposed on the main rings, while any signal from the G ring would appear at $|\tau| \leqslant 1.1$ s and be partially suppressed by our background removal procedure, which uses the delay bins at $|\tau| \geqslant 0.86$ s to define the instrumental plus sky background via Eq. (1).

4. Ring cross-sections and radial profile

In this section we calculate the average radar cross-sections of the rings for each year, examine what the radar images can tell us about the radial profile of ring reflectivity, and compare our results with those reported previously. A discussion of azimuthal variations in radar reflectivity is deferred to Section 5.

[3] In 1999, with a pulse length of 100 ms, the subradar point resolution was 16,000 km.

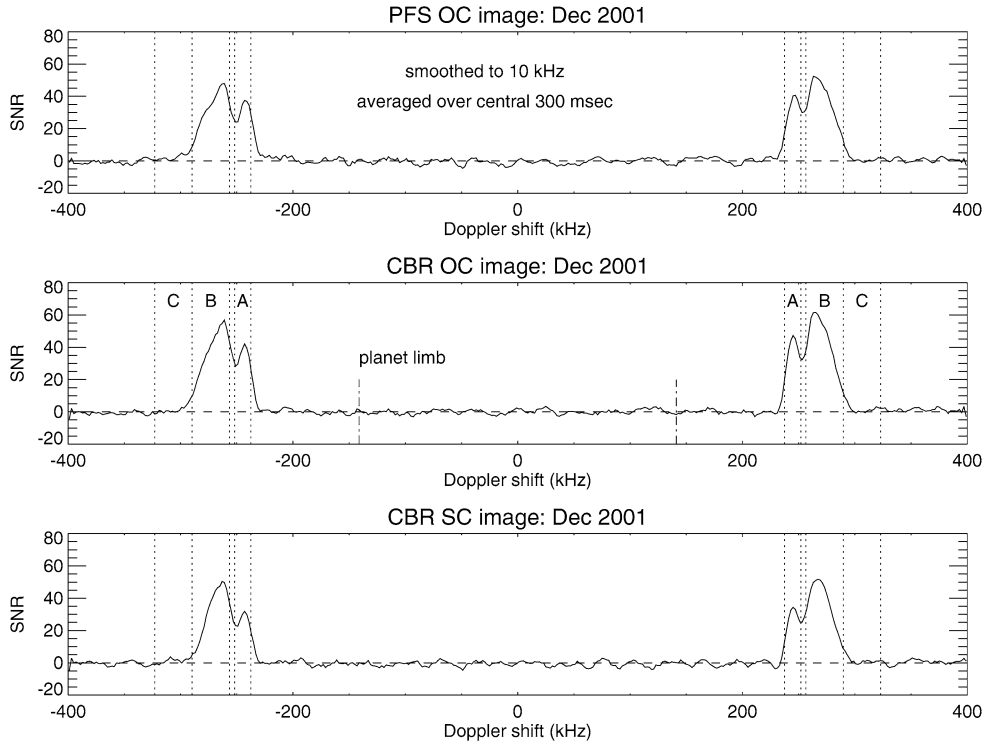

Fig. 3. Doppler spectra at zero delay, constructed from horizontal slices across the December 2001 images at the ring ansae. Predicted Doppler frequencies for echoes from the edges of the A, B, and C rings are shown by vertical dashed lines. Dot-dashed lines show the maximum Doppler shift for echoes from Saturn itself. The spectra are averaged over $\tau = \pm 150$ ms and smoothed to 10 kHz resolution. Ordinates are in units of signal to noise ratio. The three panels show the PFS (OC polarization only) and CBR (OC and SC) data separately.

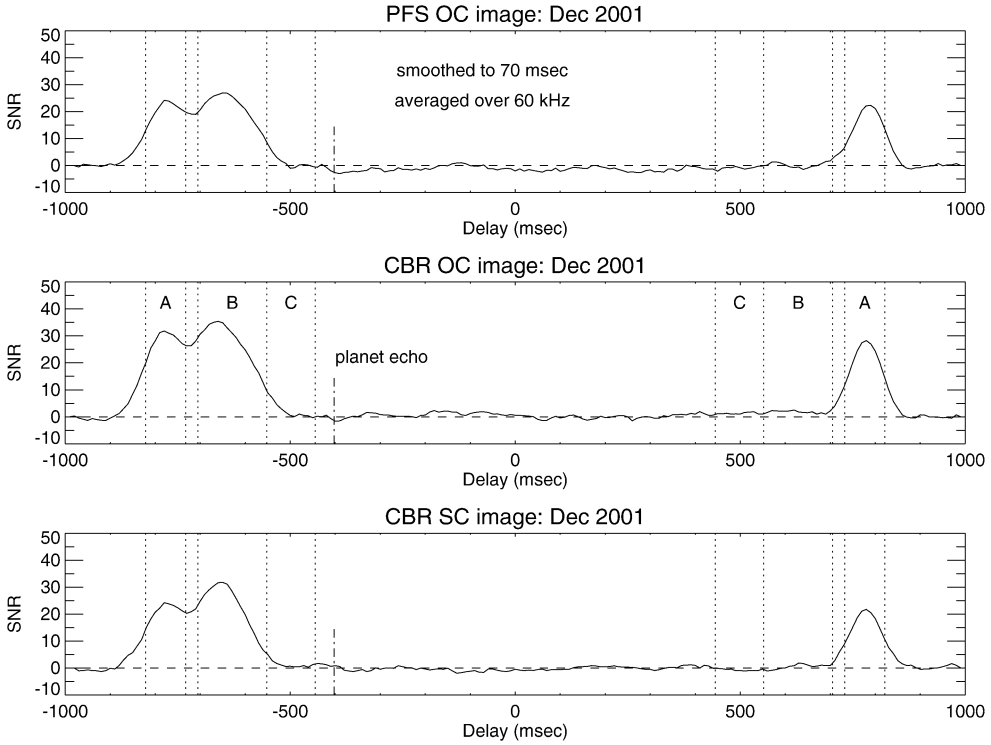

Fig. 4. Delay profiles at zero Doppler shift, constructed from vertical slices across the December 2001 images. Predicted delays for echoes from the edges of the A, B, and C rings, both in front of and behind the planet, are shown by vertical dashed lines. A dot-dashed line shows the delay for a hypothetical echo from the subradar point on Saturn itself; as expected, no such echo is seen in any of the radar images. Note the echo from the unblocked portion of the A ring beyond Saturn. Profiles are averaged over $\nu = \pm 30$ kHz and smoothed over the transmitted pulse length of 70 ms. Ordinates are in units of signal to noise ratio. The three panels show the PFS (OC polarization only) and CBR (OC and SC) data separately.

4.1. Calibration

Although the total SNR images, $I(\nu,\tau)$ are convenient for many purposes, we also wish to compute the normalized total power radar cross-section, $\hat{\sigma}_T$, and polarization ratio, μ_C, of the rings from these data for comparison with previous results. This is complicated somewhat by the frequency hopping procedure and the discrete pulses used for ranging, but the key information is contained in the image weights, W, listed in Table 3. We start with the Radar equation (Evans and Hagfors, 1968)

$$\mathrm{SNR} = \frac{P G_t G_r \lambda^2 \sigma t^{1/2}}{4\pi (4\pi D^2)^2 k T_{\mathrm{sys}} (\Delta\nu)^{1/2}}, \tag{10}$$

where P is the transmitted power, G_t, and G_r are the (dimensionless) telescope gains at the zenith angles of transmission and reception, λ is the transmitter wavelength, σ is the radar cross-section of the target, defined as the projected area of an isotropically-reflecting metallic sphere which gives the same echo strength, t is the integration time, D is the Earth–Saturn distance, T_{sys} is the receiver's system temperature, and $\Delta\nu$ is now the frequency bandwidth recorded. Substituting the round-trip light time $\tau_{\mathrm{RT}} = 2D/c$ and rewriting $G = (8\pi k g/\lambda^2) \times 10^{26}$, we obtain

$$\mathrm{SNR} = 5.48 \times 10^6 \, \frac{g_r g_t P \sigma t^{1/2}}{\tau_{\mathrm{RT}}^4 T_{\mathrm{sys}} (\Delta\nu)^{1/2}}. \tag{11}$$

Here, P is in kW, σ is in km^2, t and τ_{RT} are in s and $\lambda =$ 12.6 cm. The gain, g is now expressed in the conventional radio astronomy units of K/Jy. The radar cross-section per pixel in the images is thus

$$\sigma_{\mathrm{pix}} = 1.83 \times 10^{-7} \, \frac{\tau_{\mathrm{RT}}^4 T_{\mathrm{sys}} (\Delta\nu)^{1/2}}{g_r g_t P t^{1/2}} I(\nu,\tau). \tag{12}$$

Using the overall image weight,

$$W \simeq N_{\mathrm{snap}}^{1/2} \frac{g_t g_r P}{T_{\mathrm{sys}}} (N_{\mathrm{cyc}} N_{\mathrm{hops}})^{1/2}, \tag{13}$$

this can be conveniently expressed as

$$\sigma_{\mathrm{pix}} = 1.83 \times 10^{-7} \, \frac{\tau_{\mathrm{RT}}^4 (\delta\nu)^{1/2}}{\eta W (\delta\tau)^{1/2}} \, I(\nu,\tau), \tag{14}$$

where we have set the integration time per pixel, $t = N_{\mathrm{snap}} N_{\mathrm{cyc}} N_{\mathrm{hops}} \delta\tau$ and the bandwidth per pixel equal to the frequency resolution of the images, $\delta\nu$. The factor $\eta = 7$ accounts for the over-sampling in time delay in our images, as compared with the transmitter pulse length of 70 ms.[4]

[4] Equivalently, as the transmitter illuminated the rings at each discrete hop frequency for seven times longer than the integration time per pixel in the final images, the effective transmitted power in the radar equation must be increased by a factor of η.

4.2. Average cross-sections

To obtain the average normalized radar cross-section of the rings in either polarization we simply sum all pixels in the appropriate image and divide by the projected, unblocked area of the rings, A_{rings}:

$$\hat{\sigma} = \frac{1}{A_{\mathrm{rings}}} \sum \sigma_{\mathrm{pix}}(\nu,\tau). \tag{15}$$

In computing A_{rings} we include only the unblocked parts of the A and B rings, since no signal was detected in our images from the C ring. The calculated areas are listed in Table 4, along with $\hat{\sigma}$ for both OC and SC polarizations and the circular polarization ratio, $\mu_C = \hat{\sigma}_{\mathrm{SC}}/\hat{\sigma}_{\mathrm{OC}}$. For convenience we also list the total power normalized cross-section, $\hat{\sigma}_T = \hat{\sigma}_{\mathrm{SC}} + \hat{\sigma}_{\mathrm{OC}}$—also referred to as the 'radar albedo'—and the equivalent geometric albedo, $p = \frac{1}{4}\hat{\sigma}_T$ (Ostro et al., 1982).[5] Our results indicate that the average radar albedo of the rings has decreased by 41% as the opening angle has increased from 20.1° to 26.7°, while the polarization ratio has increased by 20%. Fig. 5 shows our estimates of $\hat{\sigma}_{\mathrm{OC}}$, $\hat{\sigma}_{\mathrm{SC}}$, $\hat{\sigma}_T$, and μ_C plotted as functions of ring opening angle, $|B|$.

The uncertainties in our cross-sections are dominated by systematic calibration uncertainties, and not by the SNR of the images. These include errors in the average transmitted power for each night, P_k, as well as in the system temperature and telescope gains, all of which enter via Eqs. (4) and (14). Values for T_{sys}, g_t, and g_r are calculated as functions of zenith and azimuth angle using polynomial expressions fitted to calibration data obtained periodically at the observatory, with T_{sys} adjusted to fit direct measurements obtained on adjacent days during radar observations of Titan or the Galilean satellites. The uncertainty in system temperature during our runs is estimated at ±2.5 K for all years, comparable to the contribution from Saturn itself when it is centered in the beam (2.75 K). The uncertainty in telescope gain is conservatively estimated at ±10%. The transmitter power at the center frequency of 2380 MHz was monitored and recorded at the start of each night's operations (see Table 2). Allowing for independent variations in average transmitter power, system temperature and telescope gain, the systematic uncertainty in the normalized cross-sections in Table 4 is estimated at ±25%. However, most of these systematic uncertainties cancel out in the calculation of μ_C, so that this quantity should be more reliably determined; the error bars in Table 4 and Fig. 5 instead reflect the statistical variations in μ_C between multiple snapshots on a single night.

We do not know why the OC cross-sections derived from the PFS and CBR data differ from each other by as much as

[5] The geometric albedo is the same quantity as the optical reflectivity usually denoted I/F, where I is the measured surface brightness of a body at zero phase angle and πF is the flux of incident sunlight at the same wavelength. The factor of 1/4 arises as the ratio of the reflectance of a smooth metallic sphere to that of a flat Lambert surface oriented normal to the incident beam.

Table 4
Average normalized ring cross-sections

	1999	2000	2001	2003
Ring opening angle, B	$-20.1°$	$-23.5°$	$-25.8°$	$-26.7°$
Ring area[a] (km^2)	8.70×10^9	10.41×10^9	11.83×10^9	12.10×10^9
$\hat{\sigma}_{\rm OC}$–PFS	–	0.44	0.39	0.37
$\hat{\sigma}_{\rm OC}$–CBR	0.76	0.55	0.43	0.42
$\hat{\sigma}_{\rm SC}$–CBR	0.49	0.41	0.32	0.32
$\mu_{\rm C}$	0.64 ± 0.06	0.75 ± 0.06	0.75 ± 0.06	0.77 ± 0.06
$\hat{\sigma}_T$	1.25 ± 0.31	0.96 ± 0.24	0.76 ± 0.19	0.74 ± 0.19
p	0.31 ± 0.08	0.24 ± 0.06	0.19 ± 0.05	0.18 ± 0.05

Note. The last three rows are calculated using the CBR data only.
[a] Projected, unblocked area of the A and B rings.

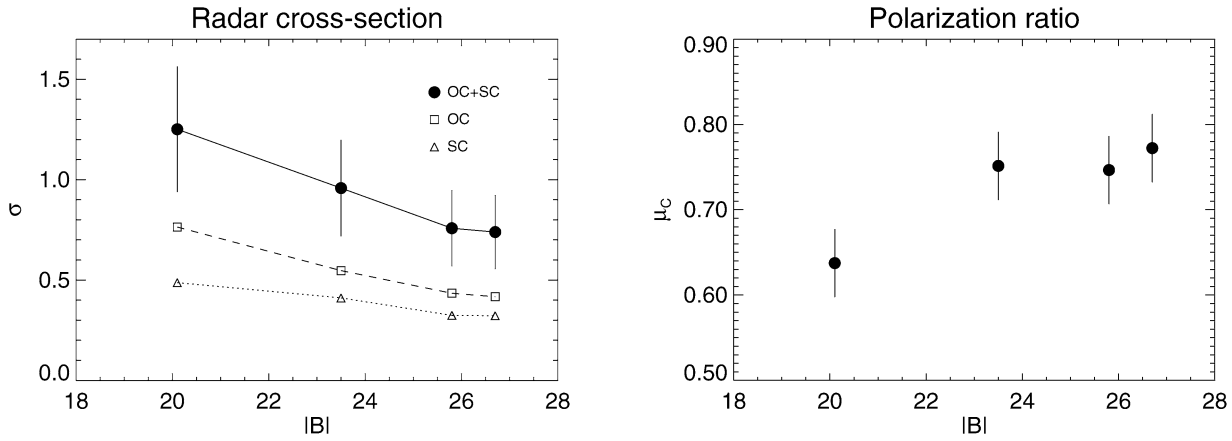

Fig. 5. Variation of the average normalized cross-sections, $\hat{\sigma}_{\rm OC}$, $\hat{\sigma}_{\rm SC}$, and $\hat{\sigma}_T$, and polarization ratio, $\mu_{\rm C}$ for Saturn's A and B rings with ring opening angle, $|B|$ between 1999 and 2003. Numerical values are given in Table 4. Uncertainties in all cross-sections are estimated at ±25%.

20% (cf. Table 4). The klystrons' power output was found to drop off significantly near the extremes of their 25 MHz bandwidths. This may be partially responsible for the systematically lower OC cross-sections obtained from the PFS data as compared to the CBR results. By integrating the measured transmitter power profiles in 2000 and 2001, we found the difference between the average and center-frequency power levels to be 3% over the 10 MHz bandwidth of the CBR, 5% over the 16 MHz PFS bandwidth in December 2001 and January 2003, and 8% over the 20 MHz PFS bandwidth used in November 2000. In addition to these transmitter power variations, potential contributors include differing amplifier gain settings for the 2-bit sampling schemes employed and differing baseband filters, though none of these seem capable of introducing differences as large as 20%. A further small reduction in signal-to-noise ratio for the PFS data in 2000 may be traceable to aliasing of noise from outside the nominal passband. In subsequent years this problem was eliminated with tunable filters. Because only the CBR data sampled both OC and SC polarizations, we have restricted the results for total power cross-sections and polarization ratios in Table 4—as well as in Table 5—to those obtained from the CBR data, but for most of the azimuthal asymmetry fits described in Section 5, we have combined the PFS and CBR data in order to maximize the signal-to-noise ratio.

4.3. Radial profiles of ring reflectivity

In addition to the average cross-sections listed in Table 4, we wish to use the radar images to determine both the radial and azimuthal variations in ring reflectivity. But because of the limited signal-to-noise ratio of the images, and particularly because of the local delay–Doppler degeneracy illustrated in Fig. 1, we have adopted a forward model-fitting approach rather than attempting to invert the observations directly. Details of the least-squares fitting algorithm are given in Appendix A, along with various tests we performed to assure its fidelity. In this section we consider the azimuthally-averaged radial profile of radar reflectivity, deferring the question of azimuthal variations to Section 5.

In our initial series of fits, we adopted a simple three-component ring model, with the C ring's inner edge set at 74,500 km, the C–B ring boundary at 92,000 km, the outer B ring edge at 117,500, and the A ring spanning the range 122,000–136,800 km. The Cassini Division, between the A and B rings, was assumed to be empty. The fitted parameters were the relative A, B, and C ring reflectivities for the OC, SC, and combined images, listed in Table 5. To avoid problems due to the systematic differences in OC cross-section between the PFS and CBR data (cf. Table 4), only the CBR data were used for these fits. We find that the ratio of A ring to B ring reflectivity has declined modestly from 0.85 ± 0.05

Table 5
Individual ring parameters

Parameter	1999	2000	2001	2003
Ring opening angle, B	$-20.1°$	$-23.5°$	$-25.8°$	$-26.7°$
A ring area[a] (km^2)	3.78×10^9	4.58×10^9	5.28×10^9	5.41×10^9
B ring area[a] (km^2)	4.92×10^9	5.83×10^9	6.54×10^9	6.69×10^9
μ_C (A ring)	0.63 ± 0.05	0.73 ± 0.05	0.72 ± 0.02	0.81 ± 0.03
μ_C (B ring)	0.70 ± 0.04	0.75 ± 0.03	0.79 ± 0.02	0.80 ± 0.02
OC polarization:				
$\hat{\sigma}$ (A ring)/$\hat{\sigma}$ (B ring)	0.89 ± 0.04	0.78 ± 0.03	0.77 ± 0.02	0.71 ± 0.02
$\hat{\sigma}$ (C ring)/$\hat{\sigma}$ (B ring)	-0.01 ± 0.05	-0.03 ± 0.04	-0.05 ± 0.02	-0.05 ± 0.03
$\hat{\sigma}_{OC}$ (A ring)	0.71	0.47	0.37	0.34
$\hat{\sigma}_{OC}$ (B ring)	0.80	0.61	0.48	0.48
SC polarization:				
$\hat{\sigma}$ (A ring)/$\hat{\sigma}$ (B ring)	0.80 ± 0.05	0.77 ± 0.04	0.69 ± 0.02	0.71 ± 0.02
$\hat{\sigma}$ (C ring)/$\hat{\sigma}$ (B ring)	-0.02 ± 0.07	-0.08 ± 0.05	-0.09 ± 0.03	-0.06 ± 0.03
$\hat{\sigma}_{SC}$ (A ring)	0.43	0.35	0.26	0.26
$\hat{\sigma}_{SC}$ (B ring)	0.53	0.46	0.38	0.37
OC + SC polarizations:				
$\hat{\sigma}$ (A ring)/$\hat{\sigma}$ (B ring)	0.85 ± 0.04	0.78 ± 0.02	0.74 ± 0.01	0.71 ± 0.02
$\hat{\sigma}$ (C ring)/$\hat{\sigma}$ (B ring)	-0.01 ± 0.04	-0.05 ± 0.03	-0.06 ± 0.02	-0.06 ± 0.02
$\hat{\sigma}_T$ (A ring)	1.14	0.82	0.63	0.60
$\hat{\sigma}_T$ (B ring)	1.34	1.06	0.86	0.85

Note. Results from 3-component least-squares fits to the CBR data. Fit uncertainties listed are 3 times the formal errors. Uncertainties in normalized cross-sections are dominated by systematic errors and estimated at 25%.
[a] Projected, unblocked area of each ring.

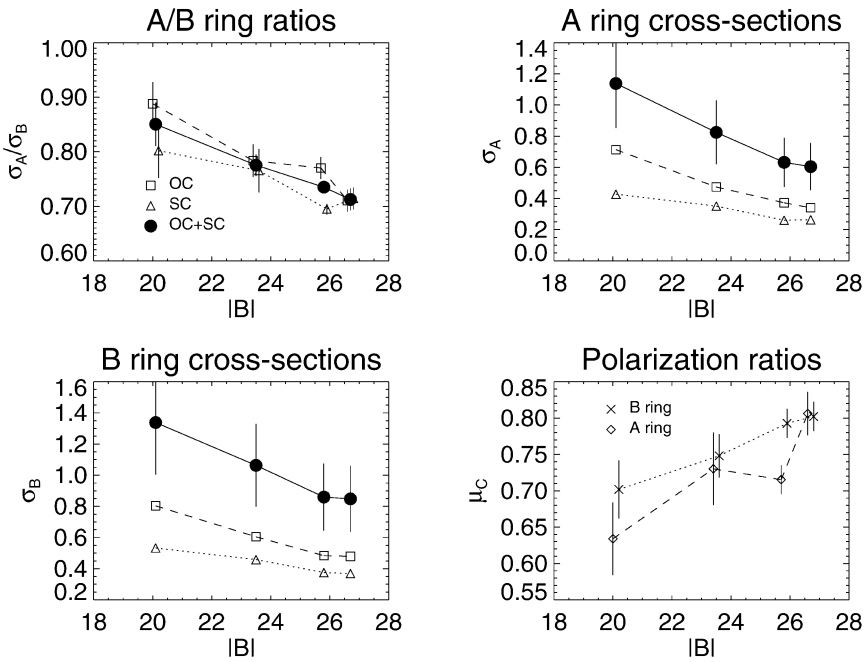

Fig. 6. Results from 3-parameter least-squares fits to the radar images in Fig. 2. Variations of the ratio of A to B ring reflectivities, individual normalized ring cross-sections, $\hat{\sigma}_{OC}$, $\hat{\sigma}_{SC}$, and $\hat{\sigma}_T$, and polarization ratios, μ_C are plotted against ring opening angle, $|B|$. Numerical values are given in Table 5. Uncertainties in all cross-sections are estimated at ±25%. Some points are shifted horizontally to avoid overlap of the error bars.

at $|B| = 20.1°$ to 0.71 ± 0.02 at $|B| = 26.7°$. As noted above, the C ring is not convincingly detected in any of the radar images. The 3-ringlet models yield 3σ upper limits to the ratio of C ring to B ring reflectivity which range from 0.04 in 1999 to 0.02 in 2001 and 2003.

Combining the average normalized ring cross-sections derived from the delay–Doppler images in Table 4 with the A/B ring ratios from the 3-ringlet models and the relative unblocked areas of the two rings, we derive the individual A and B ring normalized cross-sections also listed in Table 5 and plotted vs $|B|$ in Fig. 6. These results indicate that the radar albedos of both A and B rings have decreased as the ring opening angle has increased, by 47 and 37%, respectively. Significant decreases are seen for both OC and SC

polarizations, although the effect is more pronounced for the OC data.

The 3-ringlet models also allow us to estimate the polarization ratios for the A and B rings separately. From the fitted reflectivities, r_{SC} and r_{OC} for each year we obtain

$$\mu_C = \frac{r_{SC} W_{OC}}{r_{OC} W_{SC}}, \tag{16}$$

where the factors involving image weights arise from Eq. (14) above. The estimated values for each year are also given in Table 5 and are plotted vs $|B|$ in Fig. 6. The polarization ratios for both A and B rings appear to have increased steadily as the ring opening angle has increased, by 29 and 14%, respectively. This is in general agreement with the average increase of 20% found by summing the entire images in Table 4. There does not appear to be a statistically significant difference between μ_C for the A and B rings, though on average the B ring values are ∼5% higher.

In order to exploit the full radial resolution of the radar images, we next subdivided the A and B rings into three concentric segments each. The ringlet boundaries were based on optical depth profiles derived from the Voyager 2 PPS stellar occultation experiment (Esposito et al., 1983a), as well as similar results obtained from the 28 Sgr occultation (Nicholson et al., 2000). The B ring was subdivided into a relatively low optical depth inner region (extending out to 104,000 km), a high optical depth central region, and a slightly lower optical depth outer region (beyond 110,000 km). The A ring subdivisions were at 125,000 (inward of which the optical depth rises towards the Cassini Division) and at the Encke Gap (133,500 km). Including a uniform C ring and the Cassini Division, each model fit had 8 free parameters. Given the very similar polarization ratios found for the A and B rings in the 3-parameter fits, we restricted these fits to the combined OC + SC images and included both CBR and PFS data.

Table 6 summarizes the quantitative results of our 8-ringlet model fits, with quoted errors equal to 3 times the formal errors from the least squares fits. To set meaningful limits on the C ring's radar cross-section we prefer the results from these fits, which do a better job of matching the adjacent inner B ring than do the 3-ringlet fits. When combined with the average B ring albedos in Table 5, the model fits for 2000 to 2003 provide 3σ upper limits on $\hat{\sigma}_T$ of 0.01–0.03 for the C ring and 0.04–0.09 for the Cassini Division.

The results of the 8-ringlet fits are presented graphically in Fig. 7, superimposed on slices across the delay–Doppler images for each year at the east and west ansae (similar to the Doppler spectra in Fig. 3). This involved mapping Doppler shift into radius and taking into account the projection effects associated with the 300 ms delay width of each slice. The fitted radar reflectivities of the 8 concentric ring regions are shown as thick horizontal bars, scaled to unity for the most reflective ring segment, and also as dashed curves after smoothing to simulate the effective radial resolution of the Doppler slices. In each case, the smoothed 8-ringlet model gives a quite satisfactory match to the radial profiles derived directly from the Doppler spectra.

We note that the relative ringlet reflectivities are generally quite stable from year to year, the largest variations being seen in the inner A ring. We have also verified that the correlation coefficients between the individual ringlet reflectivities are quite low—typically $\leqslant 0.1$ and in all cases below 0.65—indicating that we are reliably retrieving radial variations in radar cross-section. The χ^2 statistics for the 8-ringlet models range from 2 to 6% lower than those of the corresponding 3-ringlet fits, with the improvement being most noticeable for the higher-quality data from 2001 and 2003.

Also shown in Fig. 7 are radial profiles of the projected filling factor of the rings,

$$F(r) = 1 - e^{-\tau(r)/\sin|B|}, \tag{17}$$

where $\tau(r)$ is the normal optical depth profile of the rings obtained from the Voyager 2 PPS stellar occultation experiment (see Nicholson et al., 2000), smoothed to 250 km resolution. If the ring's radar reflectivity is dominated by single-scattering in a many-particle-thick layer of large particles, then this expression should approximate the reflectivity profile of the rings at exactly zero phase. But in regions where interparticle scattering is important, it underestimates the dependence of reflectivity on optical depth.[6]

In fact, with a few notable exceptions, the qualitative agreement between the radar reflectivity profile and Eq. (17) is surprisingly good. The major difference occurs in the C ring, where the radar reflectivity is much smaller than predicted by the PPS data. As discussed further in Section 4.4.4, this may reflect either compositional differences or a larger population of subcentimeter-sized particles in the C ring compared to that in the A and B rings. The enhanced contrast with the A and B rings could also be due, in part, to a greater degree of multiple scattering in the more opaque regions of the rings. Similar comments apply to the consistently low radar reflectivity of the Cassini Division, a region which bears many other similarities to the C ring (Cuzzi et al., 1984).

The second-largest difference occurs in the inner B ring, where the radar reflectivity is significantly lower than might have been anticipated and is in fact comparable to that of the middle A ring. This is surprising, inasmuch as the optical depth of the inner B ring (∼1.0) is substantially higher than

[6] Further caution is warranted here, as the PPS measurements were made in the ultraviolet. However, as shown in Table 1 and Fig. 23 of Nicholson et al. (2000), the optical depth of the rings hardly varies at all between the UV and the near-IR, and is only slightly lower at centimeter wavelengths. The Voyager 1 radio occultation (RSS) data at 3.6 cm and 13 cm wavelengths might provide a better comparison with the radar reflectivities, but the RSS data are unfortunately saturated throughout the B ring and in the inner A ring (Tyler et al., 1983).

Table 6
Relative ringlet reflectivities

Parameter	1999	2000	2001	2003
Ring opening angle, B	$-20.1°$	$-23.5°$	$-25.8°$	$-26.7°$
C ring	0.03 ± 0.04	0.00 ± 0.03	0.00 ± 0.01	-0.01 ± 0.02
Inner B ring	0.70 ± 0.08	0.67 ± 0.05	0.65 ± 0.03	0.66 ± 0.03
Middle B ring	1.00	1.00	1.00	1.00
Outer B ring	0.99 ± 0.12	0.91 ± 0.07	0.91 ± 0.04	0.89 ± 0.04
Cassini Division	0.06 ± 0.13	0.00 ± 0.08	0.00 ± 0.05	0.06 ± 0.05
Inner A ring	0.71 ± 0.20	0.63 ± 0.13	0.68 ± 0.07	0.58 ± 0.08
Middle A ring	0.71 ± 0.09	0.67 ± 0.06	0.62 ± 0.03	0.61 ± 0.03
Outer A ring	0.77 ± 0.14	0.52 ± 0.08	0.51 ± 0.05	0.51 ± 0.05

Note. Results from 8-component least-squares fits to the combined OC + SC polarization images, using CBR and PFS data. Uncertainties listed are 3 times the formal errors.

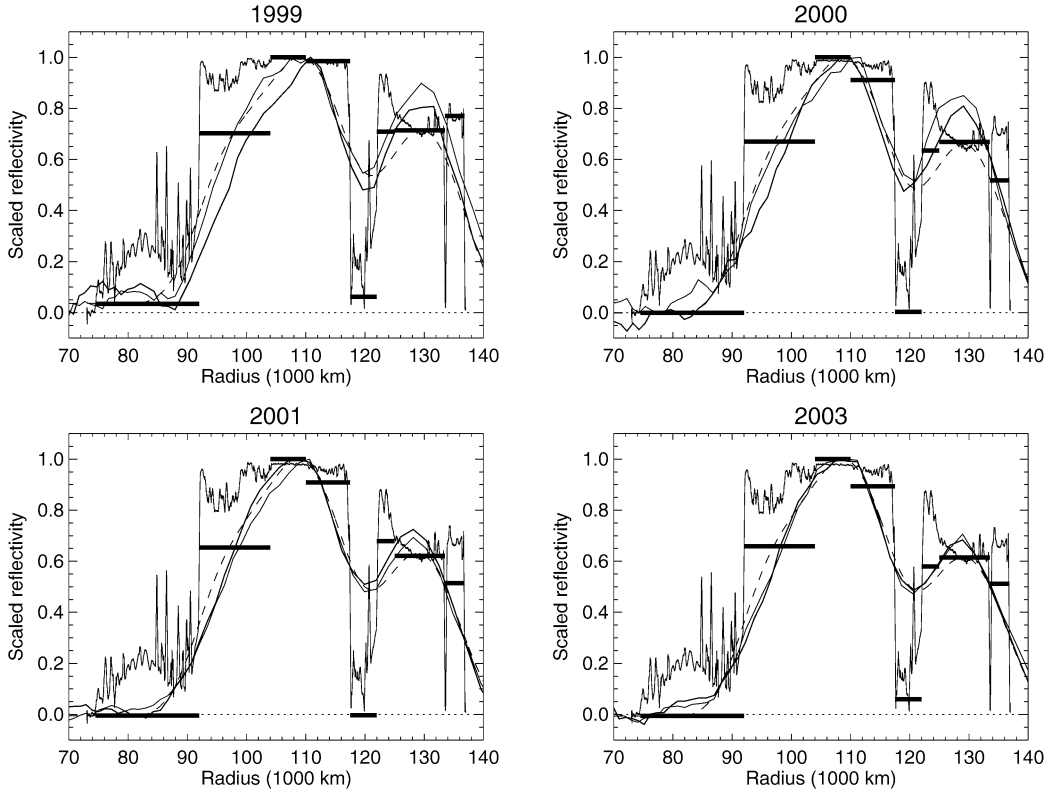

Fig. 7. Relative reflectivities for an 8-ringlet model fitted to the combined OC + SC radar images (heavy horizontal bars) superimposed on Doppler profiles for east (thick line) and west (thin line) ansae. Also shown is a profile of ring filling factor $F(r)$ derived from the Voyager PPS occultation data (see text for details). Dashed lines show the 8-component models after smoothing with a Gaussian of FWHM 10,000 km.

that of the middle A ring (∼0.5), and suggests a previously-unsuspected difference in particle properties and/or ring thickness between these two regions.

Both Voyager PPS and 28 Sgr data indicate a local maximum in optical depth in the innermost A ring at all wavelengths (cf. Fig. 13 in Nicholson et al., 2000), but this region does not show a consistently higher radar reflectivity. In the 2000 and 2003 images the radar albedo is actually lower here than in the remainder of the A ring, while in 1999 it is the same and in 2001 it is slightly higher. We do not regard any of these differences as statistically significant.

Finally, we note that, in three out of four years, the radar images show a 15–20% decrease in reflectivity outside the Encke Gap, although the optical depths on either side of the gap are quite similar, or show a slight increase (cf. Fig. 14 in Nicholson et al., 2000). Dones et al. (1993) have noted that the optical phase function of this region differs significantly from that of the rest of the A ring, and ascribe the difference indirectly to the effects of the large number of density waves in this region. They suggest either that the particles in the outer A ring have unusually smooth surfaces or that the ring itself is thicker, with both effects being due to an enhanced collision rate associated with wave damping.

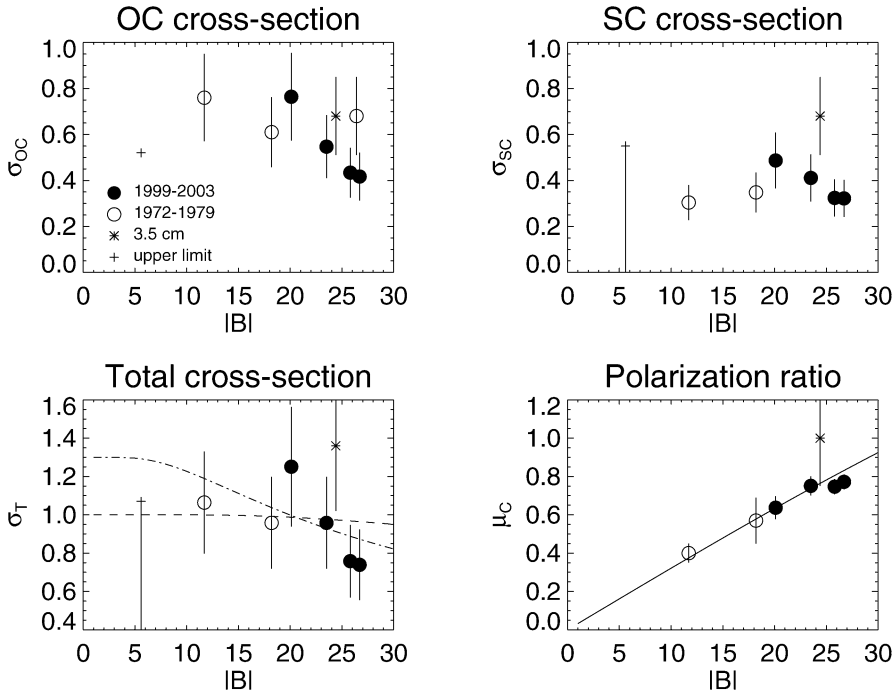

Fig. 8. Variation of average normalized ring cross-sections, $\hat{\sigma}_{\rm OC}$, $\hat{\sigma}_{\rm SC}$, and $\hat{\sigma}_T$, and polarization ratio, $\mu_{\rm C}$ with ring opening angle, $|B|$ for Saturn's rings based on all available radar data. Results from the present work are indicated by filled circles; open circles show measurements between 1972 and 1978 by Goldstein and Morris (1973), Goldstein et al. (1977), and Ostro et al. (1980), who also reported 5σ upper limits at $|B| = 5.6°$ from 1979. Asterisks denote 1974 measurements from Goldstone at 3.5 cm; all other measurements were made at 12.6 cm. Dot-dashed and dashed curves show toy monolayer models for $\hat{\sigma}_T$ from Eq. (19) for the A ring ($\tau = 0.5$) and B ring ($\tau = 1.5$), respectively. Also shown is an empirical linear fit to the polarization ratios.

4.4. Discussion

4.4.1. Comparison with previous measurements

In Fig. 8 we compare our average cross-sections and polarization ratios with previous radar measurements, as tabulated by Ostro et al. (1980). Cuzzi and Pollack (1978) made predictions of the dependence of $\hat{\sigma}_T$ on opening angle for both monolayers and many-particle-thick rings; they found a normalized cross-section which is either constant or very slowly increasing as $|B|$ increases for many-particle-thick rings with broad particle size distributions. On the other hand, monolayer models dominated by large (meter-sized) particles—made of either metal or a low-loss material with strong internal scattering—showed a steep decrease in radar albedo for $|B| \geqslant 12°$ (see their Fig. 15). Ostro et al. (1980) concluded that the available radar data ruled out the monolayer models, and favored the "thick ring" models instead, but we note that this conclusion depended heavily on their own non-detection of any echo at $B = -5.6°$ and on combining the single 3.5-cm datum at 24.5° (Goldstein et al., 1977) with 12.6-cm data at smaller opening angles.

Our estimated radar albedos are generally similar to those derived from CW observations in the 1970s, but the new data show a strong decrease in $\hat{\sigma}_{\rm OC}$ and $\hat{\sigma}_T$ between 20° and 27° for both the A and B rings which appears to be more consistent with the monolayer models. However, we note that the combined data set does not indicate such a trend, and is instead more consistent with a normalized total (OC + SC) cross-section which is independent of B, or perhaps shows a broad maximum around $|B| \simeq 15°$.

There are two previously published estimates of the rings' circular polarization ratio at 12.6 cm—$\mu_{\rm C} = 0.40 \pm 0.05$ at $B = -11.7°$ and 0.57 ± 0.12 at $B = -18.2°$ (Ostro et al., 1980)—as well as a single measurement at 3.5 cm and $B = -24.4°$ of $\mu_{\rm C} = 1.0 \pm 0.25$ by Goldstein et al. (1977). In the 1980s, these limited data led to an unresolved debate over whether the surprisingly-large value at 3.5 cm was due to the shorter wavelength (ring particles may be expected to look rougher as the wavelength approaches the size of their surface irregularities) or to the larger ring opening angle (see Ostro et al., 1980; Cuzzi et al., 1984).

As shown in Fig. 8, our own estimates are quite consistent with the previous data, and clearly confirm the increase in $\mu_{\rm C}$ with increasing $|B|$. All the 12.6 cm values fit a simple linear trend, with $\mu_{\rm C} \simeq 1.85 \sin|B|$. This fit is also marginally compatible with the lone 3.5-cm datum, which suggests that the polarization ratio depends primarily on ring opening angle and may even be independent of wavelength, though the latter conclusion clearly rests on rather tenuous ground.

4.4.2. Toy models

Previous models for the ring's radar reflectivity have usually employed one of two simple but extreme views of the rings' vertical structure. The 'classical,' or thick-ring, model is based on the concept of a cloud-like distribution

of small scatterers separated by distances which are large compared with their sizes. In this case, all shadows behind ring particles are assumed to be filled in by diffraction and the reflected intensity is given by formulae derived by Chandrasekhar (1960). The singly-scattered component of the intensity reflected back near zero phase angle is given by:

$$(I/F)_{\rm SS} = p\frac{\sin|B'|}{\sin|B'|+\sin|B|}\left(1-e^{-\tau(1/\sin|B|+1/\sin|B'|)}\right) \rightarrow \frac{p}{2}\left(1-e^{-2\tau/\sin|B|}\right) \quad \text{for } B=B', \tag{18}$$

where $p=\frac{1}{4}\varpi P(0)$ is the geometric albedo of a single ring particle, B' is the elevation of the source of illumination above the ring plane, τ is the ring's normal optical depth at the wavelength of interest, ϖ is the average particle single-scattering albedo and $P(\alpha)$ the particle phase function, normalized to an average value of unity over 4π sr. When applied at optical wavelengths, this expression must be corrected for mutual shadowing, which can lead to an opposition brightening of up to a factor of 2 (e.g., Irvine, 1966). However, it is unclear whether this applies to the radar case where the particles have sizes comparable to the wavelength of interest. The key comparison is between the length of the shadow cone, a^2/λ, and the mean spacing between particles, $D^{-1/3}a$, where D is the volume filling factor of the rings and a is the particle radius. For 10-cm-sized particles at $\lambda = 12.6$-cm shadowing is probably unimportant even in densely-packed rings, whereas for meter-sized particles some amount of shadowing will occur unless $D \ll 0.01$ (see Hapke, 1990; Cuzzi and Pollack, 1978). For the A ring, where $\tau \simeq 0.5$, expression (18) predicts a very mild decrease in $\hat{\sigma}_T$ of ∼10% as the opening angle increases from zero to 27°, while for the B ring, where the average $\tau \simeq 1.5$ at ultraviolet to near-infrared wavelengths (Nicholson et al., 2000), little if any variation of $\hat{\sigma}_T$ with $|B|$ is expected over the range accessible to Earth-based observers.[7] As noted above, when multiple scattering between particles is included the thick-ring models of Cuzzi and Pollack (1978) actually predict a slight increase in $\hat{\sigma}_T$ with ring opening angle.

The other extreme model is that of a monolayer, where shadowing becomes unimportant except at very low opening angles but where the close-packing of particles cannot be neglected. Cuzzi and Pollack (1978) assumed that for a monolayer $I/F \sim |\sin B|^{-1}$, which applies only in the no-shadowing limit. However, the very steep rise of I/F with decreasing $|B|$ implied by this formula does not hold at small opening angles ($\sin|B| < \tau/3$), where particles begin to hide one another. This is confirmed by Monte Carlo simulations of photon scattering by Salo and Karjalainen (2003) and by the analytic calculations of $I_{\rm SS}$ shown in Fig. 2 of Hämeen-Anttila and Vaaraniemi (1975). In fact, the reflectivity of a monolayer is better approximated by the projected filling factor of the ring (cf. Eq. (17) above), multiplied by the single particle albedo:

$$(I/F)_{\rm SS} = p\left(1-e^{-\tau/\sin|B|}\right). \tag{19}$$

Even this formula[8] overestimates the I/F at very small opening angles for a monolayer of Lambert spheres, where the limb-darkening of individual ring particles becomes important. For large tilt angles or low optical depths ($\sin|B| > \tau$) Eq. (19) agrees with the assumption by Cuzzi and Pollack (1978). For a singly-scattering monolayer, $\hat{\sigma}_T$ for the A ring is expected to decrease by ∼30% between $|B| = 10°$ and 27°, while the B ring is again expected to show little if any variation with $|B|$ (see Fig. 8). Multiple scattering for a monolayer increases with opening angle, as it does for a classical ring, which will again tend to counteract the decrease in I/F due to single scattering. However, the fraction of multiply-scattered signal is much less than that for a many-particle-thick layer, at least for the backscattering particles studied by Salo and Karjalainen (2003).

Thus neither the classical many-particle-thick nor the monolayer model appears able to reproduce the very steep (∼40%) decrease in $\hat{\sigma}_T$ with $|B| = 20°$–27° seen for both A and B rings in the new radar data. However, contrary to the conclusions of Cuzzi and Pollack (1978) and Ostro et al. (1980), the combined data set, which shows no unambiguous trend with B, cannot rule out either model. In Section 6 we present some new calculations for the predicted reflectivity of both classical and monolayer ring models, based on a phase function for microwave scattering by irregular particles. We find that these two very different physical models predict remarkably similar variations of radar albedo with ring opening angle. A similar conclusion was reached by Froidevaux (1981).

A more complex possibility which might account for a decrease in albedo with increasing opening angle is that the effective particle size may be a function of viewing angle. Dynamical simulations show that the larger particles tend to be concentrated near the rings' mid-plane, surrounded by a 'haze' of smaller particles (Salo, 1992b; see also Figs. 2 and 9 in Salo and Karjalainen, 2003). As a result, observations at low opening angles see primarily the smaller particles, while at larger $|B|$ we see deeper into the ring and sense the larger particles as well. According to Cuzzi and Pollack (1978), see their Fig. 8, the reflectivity of ice particles at 12.6 cm is a decreasing function of particle size for $a > 10$ cm, which could lead to a central layer of large, darker particles embed-

[7] The optical depth of the B ring was too high to measure in the Voyager radio occultation experiment, but is certainly in excess of unity at 13 cm (Tyler et al., 1983).

[8] This formula is also identical with that for a multilayer if the maximum opposition brightening at exact opposition is taken into account, which may be seen from the standard derivation of Eq. (18) in terms of incident and escape probability cylinders (see Hapke, 1986), applied to zero phase angle. Salo and Karjalainen (2003) give a formula $E_{\max} = 2/(1+\exp(-\tau/\sin|B|))$ for the maximum opposition enhancement: multiplication of Eq. (18) by this factor leads to Eq. (19).

ded within a thicker layer of small, brighter ones. We shall return to this concept below.

4.4.3. Polarization ratio and multiple scattering

The substantial depolarized (i.e., SC) echo received from the rings is indicative of a strong multiply-scattered component to the reflected signal. Our measured values of $\mu_C = 0.64$–0.77 are much larger than those typical of rocky surfaces ($\sim$0.1), though smaller than the ratios of $\sim$1.5 seen for the icy satellites Europa and Ganymede (Campbell et al., 1978; Ostro et al., 1992; Black et al., 2001) and 1.25 for the polar ice deposits on Mercury (Harmon et al., 2001). This multiple scattering could arise either within the large icy ring particles themselves (much as it does in the subsurface of Europa), or in scattering between nearby particles, or both. As the fraction of multiple scattering due to interparticle scattering is expected to increase strongly with optical depth, the similarity of μ_C for the A and B rings in Fig. 6 suggests that scattering inside the particles may dominate.

But why then should μ_C increase strongly with $|B|$ as seen in Fig. 8? If we make the usual simple assumption that the interparticle multiply-scattered echo is completely unpolarized (i.e., $\mu_C = 1$), while the singly-scattered echo is characterized by an unknown single-particle polarization ratio μ^* (cf. Cuzzi and Pollack, 1978; Ostro et al., 1980), then we have

$$\mu_C = \frac{\mu^* + \frac{1}{2}(1+\mu^*)f}{1 + \frac{1}{2}(1+\mu^*)f}, \tag{20}$$

where $f = I_{MS}/I_{SS}$. The observed increase in μ_C might be explained either by an increase in f as the ring opening angle increases or by an increase in the effective value of μ^*, as illustrated in Fig. 9. The top panel shows the variation of μ_C with f for various assumed values of μ^*, while the bottom panel shows the variation of μ^* necessary to account for the observed values of μ_C and a range of $0 < f < 1$.

From this figure we see that, for a fixed value of the single-particle polarization ratio, say 0.30, the observed increase in μ_C with $|B|$ between 12° and 27° requires approximately a tenfold increase in the multiple-scattering ratio, f. Even for $\mu^* = 0.0$, f must increase from $\sim$1.3 to $\sim$7. While the Cuzzi and Pollack (1978) thick-ring models imply a modest increase in interparticle scattering as the rings open up, these results appear to be insufficient to account for the strong variation in μ_C shown by the radar data (Ostro et al., 1980). At first glance, a monolayer ring would seem to offer even less opportunity for interparticle scattering (Cuzzi and Pollack, 1978; Ostro et al., 1980), but our own simulations of scattering by a monolayer model described in Section 6 below indicate that a substantial amount of multiple scattering is possible, at least for forward-scattering particles. However, the variation in f shown by this model also appears to be insufficient to account for the observed rapid increase in μ_C with $\sin|B|$.

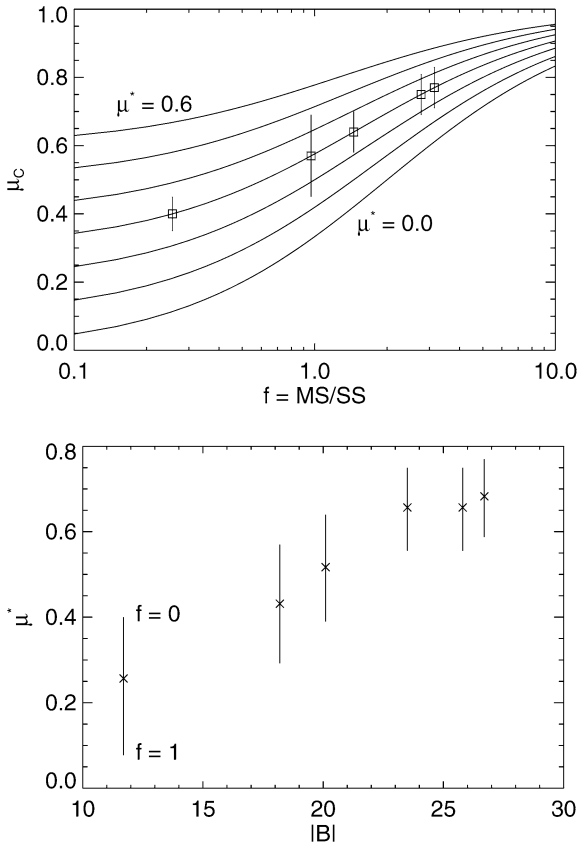

Fig. 9. (Top) Variation of the polarization ratio, μ_C with the multiple to single scattering ratio, f for assumed values of the single-particle polarization ratio, μ^* between 0.0 and 0.6, following Eq. (20). Squares correspond to the observed values of μ_C from Fig. 8 and an assumed value of $\mu^* = 0.30$. (Bottom) Variation of the single-particle polarization ratio, μ^* with ring opening angle, $|B|$ required to account for the observed polarization ratios in Fig. 8 for values of f between 0 and 1. Crosses correspond to the particular values of f derived from the Monte Carlo light-scattering calculations in Fig. 15 below for the irregular particle phase function and a dynamical optical depth of 0.5.

If interparticle scattering in either a classical or monolayer ring is unable to explain the rising depolarization with increasing opening angle, then we must appeal to an increase in μ^*, the single-particle polarization ratio, with $|B|$. As discussed in Section 4.4.2 above, this might arise in an inhomogeneous ring with larger particles concentrated towards the mid-plane. One might imagine that the more deeply buried large particles are lumpier in shape—perhaps somewhat akin to grape clusters—and thus able to depolarize in a single scattering event more effectively than can the centimeter-size particles occupying the ring 'halo.' The lower panel in Fig. 9 shows that the increase in μ^* required by the observations is approximately a factor of 3, depending on the multiple-scattering fraction and its own variation with $|B|$.

4.4.4. C ring and Cassini Division

Both our radar observations and those of Ostro et al. (1980) failed to detect any echo from the C ring, while the

Cassini Division also was not detected in our 8-ringlet least-squares models (cf. Table 6).

S-band radar experiments are largely 'blind' to particles smaller than $\sim\lambda/3 \simeq 4$ cm. Evidence for particle size variations has been summarized by French and Nicholson (2000), based on both radio and stellar occultation data. In the C ring the best-fitting power-law index is $q \simeq 3.1$, as compared with 2.75–2.9 in the A and B rings, while the diffracted signal in ground-based stellar occultation data suggests that $a_{\min}$ may be as large as 30 cm in the B and inner A rings, while $a_{\min} \leqslant 1$ cm in the C ring and Cassini Division. Both the steeper size distribution and smaller minimum size will increase the optical depth at UV-infrared wavelengths relative to that at 12.6 cm, although it remains to be seen whether these differences in the particle size distribution are sufficient to account for the very low radar cross-sections observed.

A second and perhaps more promising possibility is compositional differences. It has long been known that the particles in the C ring and Cassini Division are both darker and less red in color at visual wavelengths than those in the A and B rings (Cuzzi et al., 1984; Estrada and Cuzzi, 1996). Typical single-scattering albedos derived from Voyager imaging photometry are $\sim$0.25 in the C ring (Cooke, 1991) vs 0.4–0.6 in the A and B rings (Doyle et al., 1989; Dones et al., 1993). These variations, it has been suggested, reflect variations in the contamination of the rings' original composition of almost pure water ice by infalling meteoritic material (Cuzzi and Estrada, 1998). Near-infrared spectra also suggest the presence of small amounts of silicate and/or organic material in the C ring (Poulet et al., 2003), either of which could increase the microwave opacity and thus decrease the radar reflectivity compared with that of pure water ice.

A third possibility is that the reflectivities of the A and B rings are significantly enhanced by multiple scattering relative to that of the C ring.

5. Azimuthal asymmetries in the rings

5.1. Observations

A subtle feature of the radar images in Fig. 2 is a quadrupole asymmetry in the ring reflectivity, which is most readily seen in the peak brightness of the four 'cross-over' regions. In each image, the brightness is greater in the nearside approaching (lower right) and farside receding (upper left) quadrants than it is in the intervening quadrants. This asymmetry becomes apparent when an image from any of the four years is transposed, either in delay or in Doppler, and subtracted from itself, as shown in Fig. 10. The asymmetry appears in both OC and SC images (not shown here), as well as in the combined data. Delay profiles through the regions of peak reflectivity for each year are shown in Fig. 11, averaged over 40 kHz and smoothed to 70 ms in delay. The amplitude of the quadrupole asymmetry is similar in both polarizations, but there is a strong suggestion that it has decreased as the ring opening angle has increased. Measured as the ratio of nearside and farside peaks in such a plot, the asymmetry decreased from $\sim$1.22 in October 1999 to $\sim$1.10 in January 2003.

The mechanism whereby elongated gravitational wakes in the rings may give rise to an asymmetry in the radar reflectivity is thought to be essentially the same as that proposed at optical wavelengths. In numerical simulations (e.g., Salo, 1995; Daisaka and Ida, 1999) the wakes in the A ring have a vertical thickness (perpendicular to the ring plane) of $\sim$20 m, comparable to the average thickness of this ring (Esposito et al., 1983b). The horizontal wavelengths are comparable to the critical wavelength for axisymmetric instabilities (Toomre, 1964)

$$\lambda_{\rm cr} = \frac{4\pi^2 G\Sigma}{\kappa^2} = 70\ {\rm m}\left(\frac{r}{10^5\ {\rm km}}\right)^3 \frac{\Sigma}{100\ {\rm g\,cm^{-2}}}, \qquad (21)$$

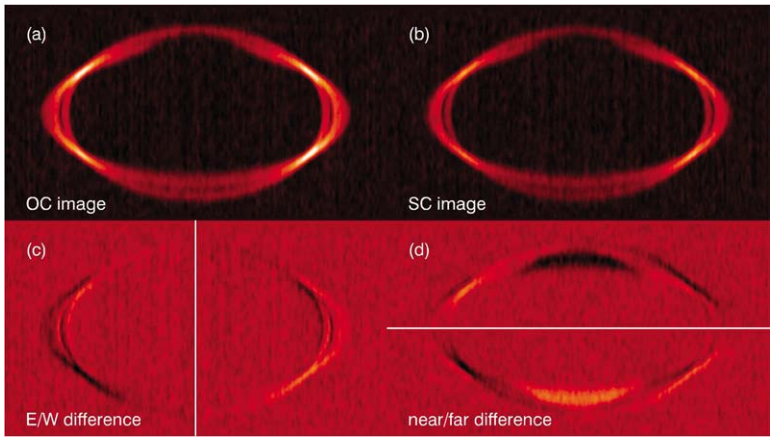

Fig. 10. (Top) Delay–Doppler images constructed from OC and SC data obtained in December 2001. (Bottom) The combined OC + SC image after transposing it in either frequency or delay and then subtracting it from the original image. Note the consistent quadrant asymmetry in the difference images: the radar echo is stronger from the far quadrant on the receding (negative Doppler) ansa and from the near quadrant on the approaching (positive Doppler) ansa.

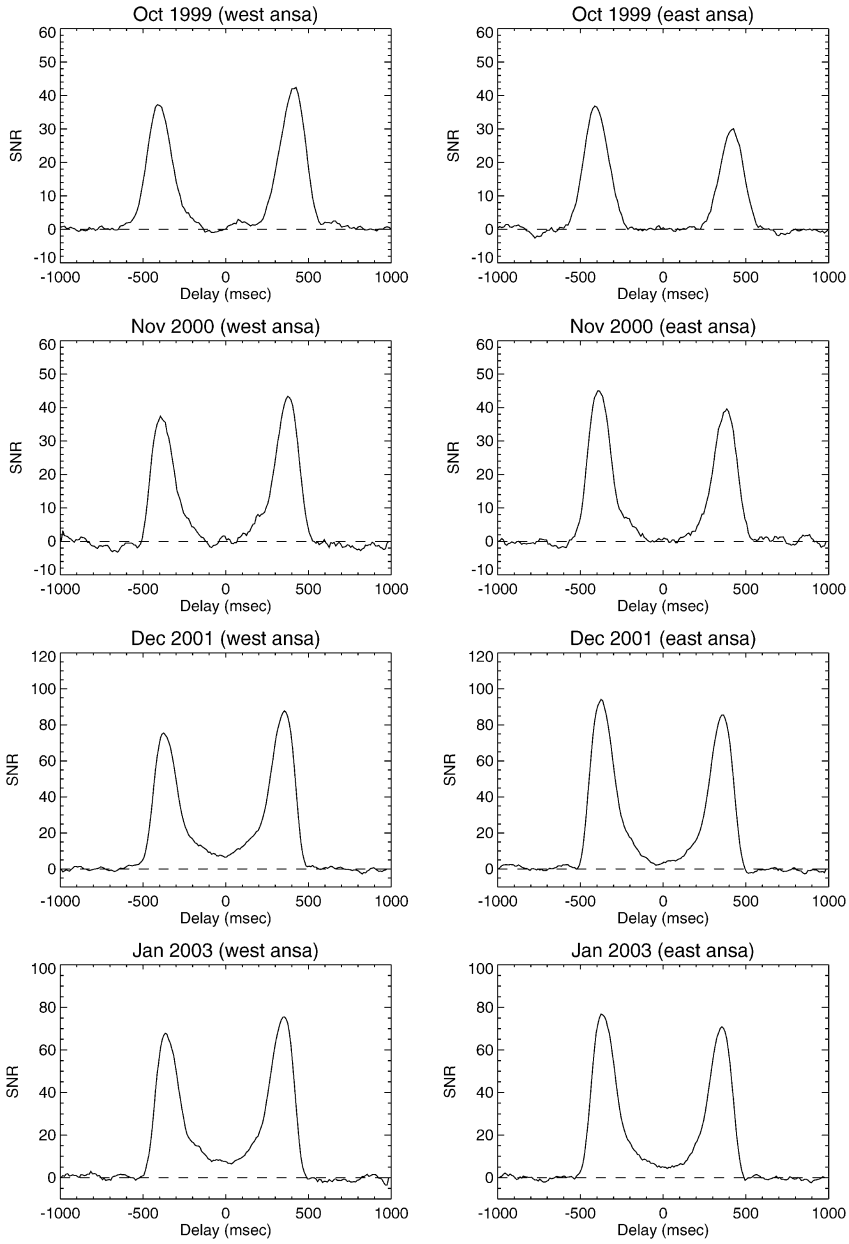

Fig. 11. Delay profiles through the four bright features in each image in Fig. 2, showing how the near/far brightness asymmetry consistently changes sign between east (approaching) and west (receding) ansae. Profiles are averaged over the frequency range $200 \leqslant |\nu| \leqslant 240$ kHz and smoothed over 70 ms. Ordinates are in units of signal to noise ratio. There is a modest decrease in amplitude of the asymmetry between 1999 and 2003.

where r is the ring radius, Σ is the surface mass density and $\kappa \simeq \Omega$ is the local epicyclic frequency of ring particle orbits. In the middle A ring, we have $\Sigma \simeq 45\,\mathrm{g\,cm^{-2}}$ and $\lambda_{\mathrm{cr}} \simeq 75$ m. At ring opening angles of $|B| \leqslant 15°$ the wakes will thus appear to overlap when viewed transversely, and the ring will appear solidly filled with scatterers. When the wakes are viewed on-axis, however, the radar beam will 'see' the low density regions between them and the average cross-section of the rings will be lower. Since the wakes trail at an average angle of $\sim 21°$ relative to the azimuthal direction in a Keplerian ring (Julian and Toomre, 1966), they are seen on-axis $\sim 21°$ in longitude preceding elongation, in agreement with the observed sense of the radar quadrupole asymmetry.[9] This is illustrated by the cartoon in Fig. 12, from Salo et al. (2004). As the opening angle increases above $\sim 15°$, the gaps between the wakes should become increasingly visible and the amplitude of the asymmetry is predicted to decrease. Conversely, at very low opening angles the ring will appear more opaque at all longitudes and the asymmetry should

[9] The pitch angle of wakes is actually somewhat variable. Both wakes due to an embedded mass, as displayed by Julian and Toomre (1966), and the autocorrelation plots from the simulations by Salo et al. (2004) show pitch angles which decrease outwards from 25–30° to an asymptotic value of $\sim 15°$. The value of 21° adopted here is an effective pitch angle averaged over the wake.

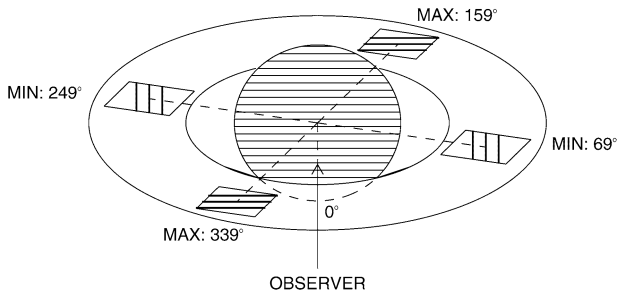

Fig. 12. Cartoon illustrating how an azimuthal asymmetry in ring reflectivity can arise from elongated wakes trailing at an angle of 21°. Near longitudes of 69° and 249° from the sub-Earth point, the observer sees the wakes end-on as well as the lower-density intervening regions. But because the vertical thickness of the wakes of ∼20 m is comparable to their spacing of ∼75 m, the wakes largely appear to overlap at longitudes near 159° and 339°, resulting in a higher average cross-section. From Salo et al. (2004).

again decrease. Models by Salo and Karjalainen (1999) and Salo et al. (2004) predict that the maximum asymmetry will occur at $|B| \simeq 12°$, as observed at optical wavelengths.

Unfortunately, a singularity in the transformation from delay–Doppler coordinates to spatial coordinates in the ring plane associated with the degeneracy illustrated in Fig. 1 prevents converting the images in Fig. 2 directly into profiles of reflectivity vs ring longitude.[10] It is thus not possible to produce a plot of the radar quadrupole asymmetry analogous to those which illustrate the well-known azimuthal asymmetry seen in the A ring at optical wavelengths. Moreover, this degeneracy mixes echoes from the A and B rings at just those longitudes where the brightness asymmetry is most pronounced (cf. Fig. 1), making it difficult to see from the images in which ring the asymmetry resides. As in the case of radial albedo variations, our approach is instead to fit a model incorporating the anticipated brightness variations to the radar images.

5.2. *Model fits*

To estimate the azimuthal asymmetry of the radar ring brightness, we included additional components in our multiple-ringlet model based on numerical light scattering calculations for N-body representations of gravitational wakes, as described by Salo et al. (2004). The azimuthal variation in ring brightness was computed at zero phase angle and for values of $|B|$ appropriate to the radar observations, using a Monte Carlo ray tracing scheme based on geometric optics and incorporating multiple-scattering (Salo and Karjalainen, 2003). We assumed for simplicity a photometric 'reference model' employing a Lambert sphere phase function with $\varpi = 1.0$, but permitted the amplitude of the model asymmetry to vary in order to achieve the best fit to the radar data. Additional models with more realistic microwave phase functions are discussed in Section 6.

We allowed for independent asymmetries in both A and B rings (although the effect seems to be confined largely to the A ring at optical wavelengths), as well as uniform background reflectivities for the A, B and C rings, as before. The fitted azimuthal asymmetry amplitude was parameterized via the quantity

$$\beta = \frac{I_{\max} - I_{\min}}{I_{\max} + I_{\min}}. \tag{22}$$

For the reference model, which was computed with parameters appropriate to the middle A ring, the asymmetry amplitude decreases monotonically from $\beta = 0.13$ for $|B| = 20°$ to 0.10 at 26°. These values are in quite good agreement with the maximum asymmetry observed in the A ring in HST images taken during this period (French et al., in preparation).

When fitted to the radar images obtained between 2000 and 2003,[11] this model yields substantial asymmetry amplitudes for the A ring, but much smaller and somewhat variable amplitudes for the B ring, as shown in Table 7. The A ring asymmetry decreases monotonically from $\beta = 0.21 \pm 0.03$ in 2000 to 0.16 ± 0.02 in 2003—which is at least 50% greater than the reference model predicts at these times—while that of the B ring ranges from a high of ∼0.08 in 2000 to a low of ∼0.03 in 2001.

A limitation of the above fits is that they assume that the azimuthal reflectivity profile has its minima at the longitudes given by the gravitational wake model, i.e., at $\theta \simeq 69°$ and 249°.[12] A more robust test of the model is to allow the asymmetry pattern to rotate freely in longitude and to find the orientation that gives the best fit to the data. In practice, we implemented this test in two ways. First, we constructed separate asymmetry models for the A ring in which the model profile was rotated in steps of 15° of orbital longitude. We fitted each of these separately, with the results shown in Fig. 13. In the left panel, the amplitude of the asymmetry is plotted as a function of the longitude of the minimum brightness of the model, $\theta_{\min}$. The right panel shows the RMS residuals for each fit, scaled to unity for the best fit so that all three years' results can be compared in the same figure. The smooth curves are spline fits to the discrete fit results. In each case, the best fit is obtained for $\theta_{\min} \simeq 70°$, as expected for gravitational wakes.

In order to obtain a quantitative estimate of the uncertainty in the phase, in our final series of fits we included two $m = 2$ asymmetry components for the A ring, phase shifted by 45° relative to one other in longitude. (Although the parts of the rings blocked by the planet spoil the anticipated orthogonality of these two components, the correlation

[10] An attempt at creating such a profile was made, after heavy oversampling of the radar images, but with disappointing results.

[11] Possible telescope pointing errors in 1999 introduced a significant E–W brightness asymmetry into these images which makes it difficult to get reliable fits for the azimuthal asymmetry for this year.

[12] The ring longitude, θ is measured in a prograde direction from the sub-Earth point.

Table 7
Azimuthal asymmetry parameters[a]

Parameter	2000	2001	2003
Ring opening angle, B	$-23.5°$	$-25.8°$	$-26.7°$
Reference simulation: A ring			
β	0.113	0.103	0.103
$\theta_{\min}$	67.6	67.0	67.0
A and B ring asymmetries[b]			
β (A ring)	0.212 ± 0.033	0.172 ± 0.020	0.156 ± 0.021
β (B ring)	0.079 ± 0.022	0.027 ± 0.013	0.044 ± 0.013
A ring asymmetry only			
A ring CBR data: OC polarization:			
β	0.19 ± 0.04	0.19 ± 0.03	0.18 ± 0.03
$\theta_{\min}$	$70 \pm 12°$	$75 \pm 9°$	$61 \pm 11°$
A ring CBR data: SC polarization:			
β	0.25 ± 0.05	0.25 ± 0.03	0.19 ± 0.03
$\theta_{\min}$	$73 \pm 12°$	$69 \pm 8°$	$66 \pm 10°$
A ring CBR data: OC + SC polarizations:			
β	0.22 ± 0.03	0.21 ± 0.02	0.19 ± 0.02
$\theta_{\min}$	$71 \pm 9°$	$72 \pm 7°$	$64 \pm 8°$
A ring: combined data set, OC + SC polarizations:			
β	0.24 ± 0.03	0.18 ± 0.02	0.18 ± 0.02
$\theta_{\min}$	$71 \pm 8°$	$66 \pm 6°$	$63 \pm 7°$

Note. Except as noted, all fits are to the combined PFS and CBR data, including both polarizations. Fit uncertainties listed are 3 times the formal errors.

[a] The asymmetry amplitude is defined as $\beta = (I_{\max} - I_{\min})/(I_{\max} + I_{\min})$. $\theta_{\min}$ is the longitude of minimum reflectivity, measured from the observer in the prograde direction.

[b] Fits assume reference values for $\theta_{\min}$.

coefficient between them is still quite low.) For these fits the B ring was assumed to be azimuthally uniform in order to reduce the number of free parameters, and we performed fits to the SC and OC CBR images separately, as well as to the total CBR images and to the combined data set. The fitted amplitudes, β and phases, $\theta_{\min}$ are given in Table 7.

Dones et al. (1993) found that the amplitude of the azimuthal asymmetry in Voyager images was strongly peaked in the middle A ring, at a radius of ∼130,000 km. An attempt was thus made to further localize the azimuthal asymmetry in the radar images by adding separate asymmetry components for each of the six A and B ringlets in the 8-component ring model described in Section 4.3 above. However, large negative correlations between the amplitudes in adjacent ringlets made it impossible to draw any robust conclusions from these fits and we do not show any of these results here.

Finally, we note that the fitted asymmetry amplitudes are quite sensitive to the antenna beam profile. This arises because the beam FWHM is only ∼3 times the major diameter of the ring system, combined with the fact that the longitudes of minimum brightness are within 20° of the ring ansae. Model fits which neglect the beam profile yield even larger A ring asymmetries of $0.21 \leqslant \beta \leqslant 0.26$.

We may summarize the results in Fig. 13 and Table 7 as follows.

1. The average A ring asymmetry amplitude in the radar images is a factor of 1.5–2 times higher than the reference wake model predicts at optical wavelengths, using a conservative Lambert-sphere particle phase function, or what is seen in contemporaneous HST images.
2. The average observed longitude of minimum brightness, $\theta_{\min} = 67 \pm 4°$ agrees very well with the wake model, even though this model was not optimized in any way to fit the radar data. The numerical wake model predicts that $\theta_{\min} = 67$–$68°$ in 2000–2003.
3. The amplitude of the asymmetry was appreciably lower in 2001 and 2003 at $|B| \simeq 26°$ than it was in 2000, when $|B| = 23.5°$, also in qualitative agreement with the wake model.
4. The asymmetry is clearly present in both SC and OC images, but is ∼20% stronger in the SC images from 2000 and 2001 (cf. Table 7).
5. There is a much smaller but statistically-significant (at least 6σ) asymmetry in the B ring.

The relatively small fitted amplitude of the azimuthal asymmetry in the B ring raises the possibility that this may be due to contamination from the A ring, especially as the two rings partially overlap in the delay–Doppler images. However, Table 8 shows that the correlation coefficient between the A and B ring amplitudes is a modest −0.27. Moreover, a similar asymmetry has been seen at a low level in the contemporaneous HST data (French et al., in preparation), where it is seen to be largely confined to the lower optical depth inner B ring. These results are supported by a few numerical wake models which have been calculated for the B ring ($r = 100{,}000$ km), which suggest a likely amplitude of 0.02–0.04 at $|B| = 20°$, similar to that seen in the 2001 and

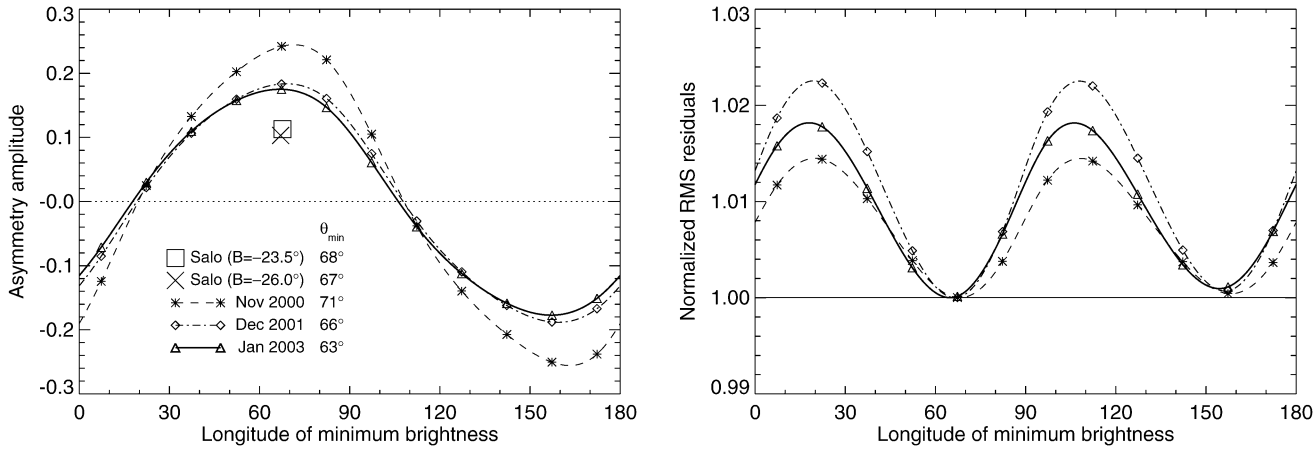

Fig. 13. Variation of the fitted asymmetry amplitude, β (left panel) and RMS fit residuals (right panel) with the assumed longitude of minimum A ring brightness $\theta_{\min}$. Separate curves show fits to the OC + SC images from 2000, 2001, and 2003. The amplitude has decreased from 0.24 ± 0.03 in November 2000 to 0.18 ± 0.02 in January 2003, while the best-fit values of $\theta_{\min}$ varied from 71° to 63° (see Table 7). The large square and cross show the amplitude and phase at optical wavelengths as predicted by simulations of gravitational wakes (Salo et al., 2004).

Table 8
Correlation coefficients

Parameter	$\hat{\sigma}$ (C ring)	$\hat{\sigma}$ (B ring)	$\hat{\sigma}$ (A ring)	β (A ring)	β (B ring)
			2000		
$\hat{\sigma}$ (C ring)	1.00	−0.30	−0.01	0.02	0.05
$\hat{\sigma}$ (B ring)		1.00	−0.26	−0.01	0.21
$\hat{\sigma}$ (A ring)			1.00	0.09	−0.09
β(A ring)				1.00	−0.27
β(B ring)					1.00
			2001		
$\hat{\sigma}$ (C ring)	1.00	−0.31	−0.01	0.02	0.04
$\hat{\sigma}$ (B ring)		1.00	−0.25	−0.00	0.22
$\hat{\sigma}$ (A ring)			1.00	0.06	−0.08
β (A ring)				1.00	−0.27
β (B ring)					1.00
			2003		
$\hat{\sigma}$ (C ring)	1.00	−0.31	−0.01	0.02	0.04
$\hat{\sigma}$ (B ring)		1.00	−0.25	−0.00	0.20
$\hat{\sigma}$ (A ring)			1.00	0.06	−0.07
β (A ring)				1.00	−0.27
β (B ring)					1.00

Note. Correlation coefficients for 5-component least-squares fits to the combined OS + SC images, using both CBR and PFS data.

2003 radar images. However, these calculations also predict a similar asymmetry in the outer B ring, which is not observed in the HST images.

5.3. Discussion

Other evidence for the influence of gravitational wakes on microwave scattering in Saturn's rings has been presented by Molnar et al. (1999) and Dunn et al. (2004), who observed an azimuthal gradient in the optical depth of the A ring where it was seen silhouetted against the planet, consistent with the varying projected orientations of wakes in this ring. As expected, no such variation was seen in the C ring. Van der Tak et al. (1999) also ascribed an east–west asymmetry between the ring ansae observed at $B \sim -20°$ to emission from Saturn being more readily reflected from, rather than transmitted through, high optical depth trailing wakes. However, this particular EW asymmetry was strongest in the C and B rings and weak or non-existent in the A ring where gravitational wakes are expected to be developed most strongly.

A clue to the origin of the unexpectedly large radar asymmetry is provided by the rings' polarization ratio, μ_C, with its implication that a significant fraction of the radar echo has been multiply-scattered. This is likely to remain true even if part of the increase in μ_C with opening angle is due to variations in μ^*, as suggested in Fig. 9. The observation that the asymmetry is larger in the SC polarization images than it is for the OC polarization (cf. Table 7) also suggests that multiple scattering may play a significant role. At microwave frequencies, water ice particles are largely transparent and moderately forward-scattering (Cuzzi and Pollack, 1978; see their Fig. 13). More of the reflected radar signal is thus likely to arise from multiple scattering between nearby ring particles than is the case at optical wavelengths, where the reflectivity of the rings near zero phase angle is overwhelmingly dominated by single scattering (Dones et al., 1993). (At optical wavelengths ($x = 2\pi a/\lambda \gg 1$) centimeter-to-meter-sized ring particles behave as small, opaque, frost-covered satellites which are highly back-scattering.) Because multiple scattering is a much stronger function of optical depth than is single scattering—scaling roughly as $\sim\tau^2$—it is expected to accentuate the difference between the denser wake and more tenuous 'interwake' regions. This could in turn result in an enhanced azimuthal asymmetry at microwave wavelengths. In the next section, we develop a simple radiative transfer model for the A ring based on these ideas which may be capable of accounting for the observed radar asymmetry amplitude.

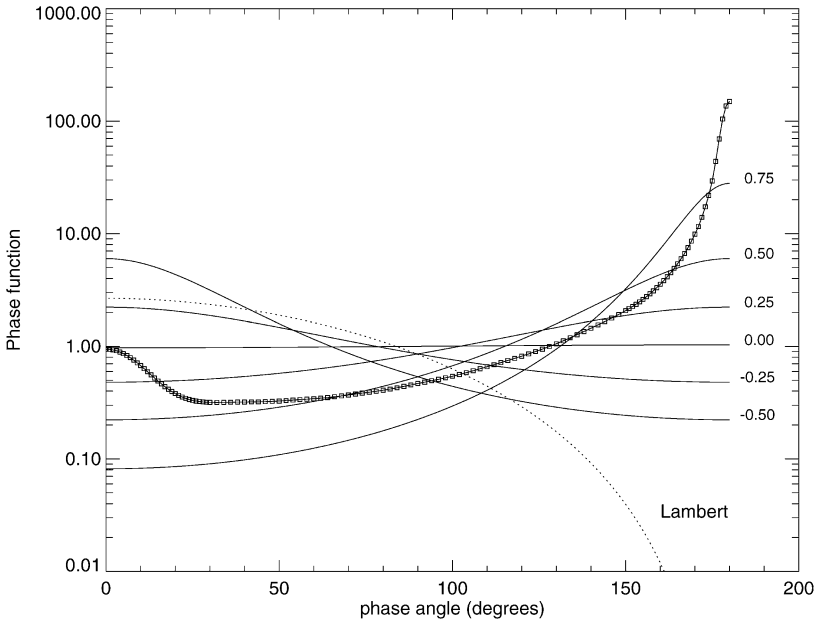

Fig. 14. A series of Henyey–Greenstein phase functions, $P(\alpha)$, parameterized by the asymmetry parameter $g = -\langle\cos\alpha\rangle = -0.50, -0.25, 0.01, 0.25, 0.50$, and 0.75, compared with an average ring particle phase function at a wavelength of 12.6 cm (denoted by squares) computed using a composite Mie scattering/irregular particle model for pure water ice particles with a $q = 3$ power-law size distribution between radii of 1 and 100 cm. The particles' complex refractive index $n = 1.78 + 6 \times 10^{-6} i$ and the shape parameter $x_0 = 8$ (Cuzzi and Pollack, 1978). For the irregular particle model, $g = +0.53$. The dotted curve shows the phase function for a Lambert sphere ($g = -0.44$), as used to compute our reference wake asymmetry model.

6. A radiative transfer model for the A ring

Although a full study of the scattering properties of the rings at microwave frequencies is beyond the scope of this paper, and should incorporate recent thermal emission and scattering observations as well as radar data, we have performed some limited calculations using the same dynamical simulations of wakes in the A ring by Salo et al. (2004) used for the asymmetry model fits in Section 5. In the context of the toy models discussed in Section 4.4.2 above, this model may be thought of as a near-monolayer, inasmuch as the full thickness of the ring of 10 m is only ∼3 times the particle diameter. It is, however, a fully 3-dimensional simulation which incorporates both particle self-gravity and collisions. The dynamical optical depth of the ring is 0.5, and the mean surface mass density is 50 g cm^{-2}, both appropriate to Saturn's middle A ring.[13] As in Section 5, the distribution of radiation scattered from the ring is calculated using the Monte Carlo light-scattering code described by Salo and Karjalainen (2003), but here we use a more realistic phase function for microwave scattering by irregular water ice particles. Our goal is primarily to account for the large amplitude of the azimuthal asymmetry seen in the radar data.

The semi-empirical phase function we employ was developed originally by Cuzzi and Pollack (1978) and modified and used extensively by later authors (Dones et al., 1993; Showalter et al., 1992; Showalter and Cuzzi, 1993). It is a composite of Mie scattering and irregular particle phase functions, computed for our observing wavelength of 12.6 cm and for a power-law particle size distribution between radii of 1 and 100 cm, typical of those obtained by Marouf et al. (1983) and French and Nicholson (2000). It is compared in Fig. 14 with the Lambert sphere phase function used for the least-squares models in Section 5 and a suite of Henyey–Greenstein phase functions, such as are commonly used in optical light scattering models of the rings. Note that the semi-empirical phase function exhibits both weak back-scattering and strong forward-scattering lobes, the latter due to a combination of transmission and diffraction. An overall measure of the directionality of a phase function is provided by the anisotropy parameter g, the average of the cosine of the scattering angle. For our semi-empirical model $g = +0.53$, whereas for a Lambert sphere $g = -0.44$ and for the highly back-scattering Callisto phase function $g = -0.55$. The Henyey–Greenstein models in Fig. 14 span this range.

Observations of passive radio 'emission' from Saturn's rings (actually, scattered thermal radiation from Saturn) confirm that the ring particles are indeed forward scattering (Grossman et al., 1989; de Pater and Dickel, 1991; Van der Tak et al., 1999; Dunn et al., 2002), as demonstrated by front-to-back asymmetries in the brightness of the C and B rings especially. Dunn et al. (2002) successfully modeled these asymmetries at $B = +2.7°$ and $-5°$ using a composite Mie scattering model for centimeter-to-meter-sized ice particles with an admixture of isotropic scattering to simulate the influence of particle roughness at shorter wavelengths.

[13] The dynamical optical depth, $\tau_{\rm dyn}$ is defined as the total geometric area of ring particles per unit surface area of the rings, as seen at normal incidence, or $\int_0^\infty \pi a^2 n(a)\,{\rm d}a$, where $n(a)$ is the differential particle size distribution.

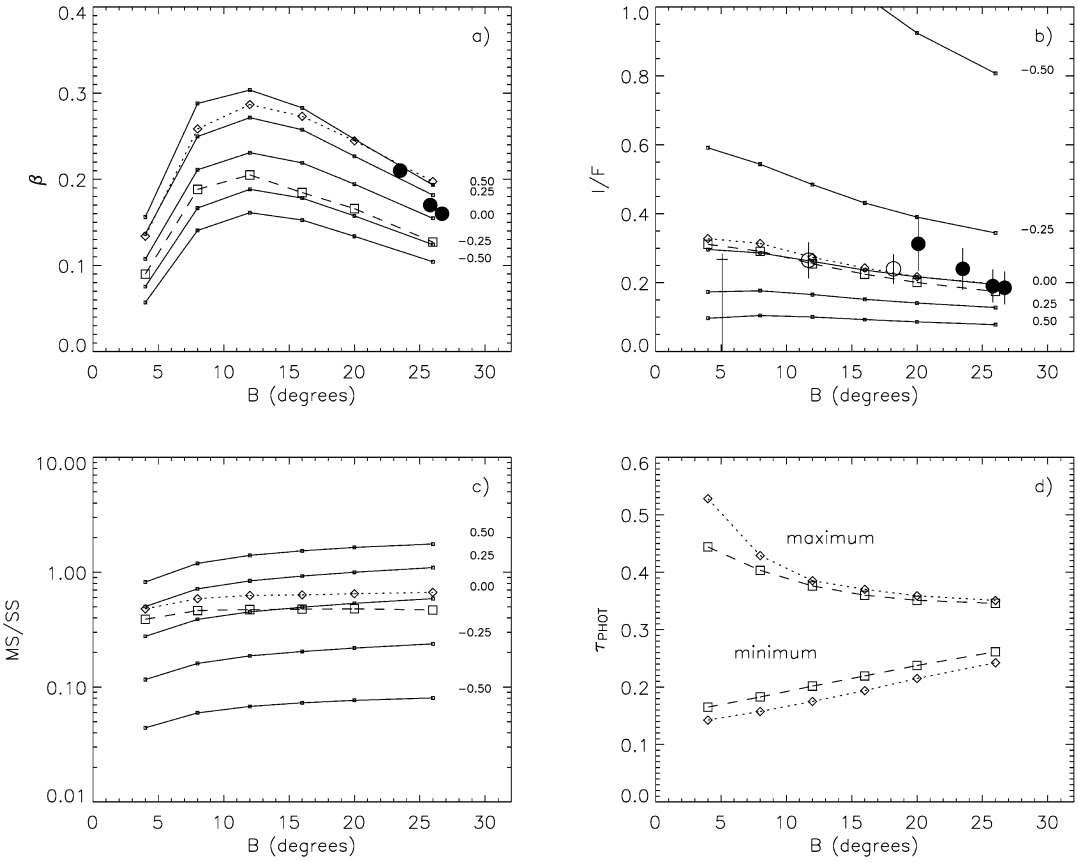

Fig. 15. Predicted variations in (a) azimuthal asymmetry amplitude, β, (b) average reflectivity, I/F, and (c) multiple to single scattering ratio vs ring opening angle at zero phase angle for the A ring, based on the particle phase functions shown in Fig. 14. The underlying dynamical simulation is that of Salo et al. (2004), with a particle radius of 1.67 m and a particle density of 0.45 g cm^{-3}. Solid lines correspond to Henyey–Greenstein phase functions with $-0.5 < g < 0.5$ and a dynamical optical depth, $\tau_{\rm dyn} = 0.5$. Dashed and dotted lines are calculated using the irregular particle phase function and dynamical optical depths of 0.5 and 0.8, respectively. Note that the peak asymmetry occurs for $|B| \simeq 12°$ regardless of phase function, while the average reflectivity decreases with increasing elevation angle. Open and filled circles show the observed radar asymmetries for the A ring (from Table 7) and the average geometric albedos, $p = \hat{\sigma}_T/4$ (from Table 4), using the same symbols as in Fig. 8. Panel (d) shows the range in photometric optical depth with ring longitude due to the wakes, for $\tau_{\rm dyn} = 0.5$ and 0.8.

They attributed the apparent lack of forward scattering in the A ring to near-field effects between the particles.

The Monte Carlo model permits the different orders of photon scatterings to be tabulated separately, and the results confirm our expectation above that multiple-scattering will enhance the azimuthal asymmetry. For a wide range of values for the parameter g, we find that the amplitudes of the asymmetry in the doubly- and triply-scattered signal are approximately twice that in the singly-scattered signal (see also Fig. 14 in Salo et al., 2004). For quadruple scattering, the asymmetry is roughly three times larger than that for single scattering. In order to explore the role of the phase function in determining the azimuthal asymmetry amplitude, we carried out a series of runs based on the same dynamical simulation using both the semi-empirical irregular particle phase function as well as the set of Henyey–Greenstein phase functions with anisotropy parameter $-0.5 \leqslant g \leqslant 0.5$ shown in Fig. 14. The resulting variations in azimuthal asymmetry, β, average reflectivity, I/F, and multiple scattering ratio, f, with ring opening angle are shown in Fig. 15.

As expected, the asymmetry amplitude increases monotonically as g increases (i.e., as forward scattering becomes increasingly important), due to the increased fraction of multiple scattering. For $|B| = 26°$ and $g = -0.5$ (similar to Callisto or a Lambert sphere) $\beta = 0.104$, whereas for $g = 0$ (isotropic scatterers) $\beta = 0.155$ and for $g = +0.5$ we find $\beta = 0.193$, comparable to the observed value in Table 7. The corresponding ratios of multiple to single-scattering are 0.08, 0.6, and 1.8, respectively. The irregular particle model has both back-scattering and forward-scattering lobes which act to reduce the fraction of multiple scattering at zero phase angle in comparison with a single-lobed Henyey–Greenstein function with a similar value of g. As a result, its asymmetry amplitude at $|B| = 26°$ is only 0.127, even though $g = +0.53$ for this phase function. This is significantly less than the observed value of $\sim$0.18, but we note that this is simply one particular model which has not been 'tuned' to fit the data. An extension of the particle size distribution to a maximum radius of 10 m, for example, will strengthen the forward-scattering lobe and should increase the asymmetry amplitude. Or an increase in the surface mass density

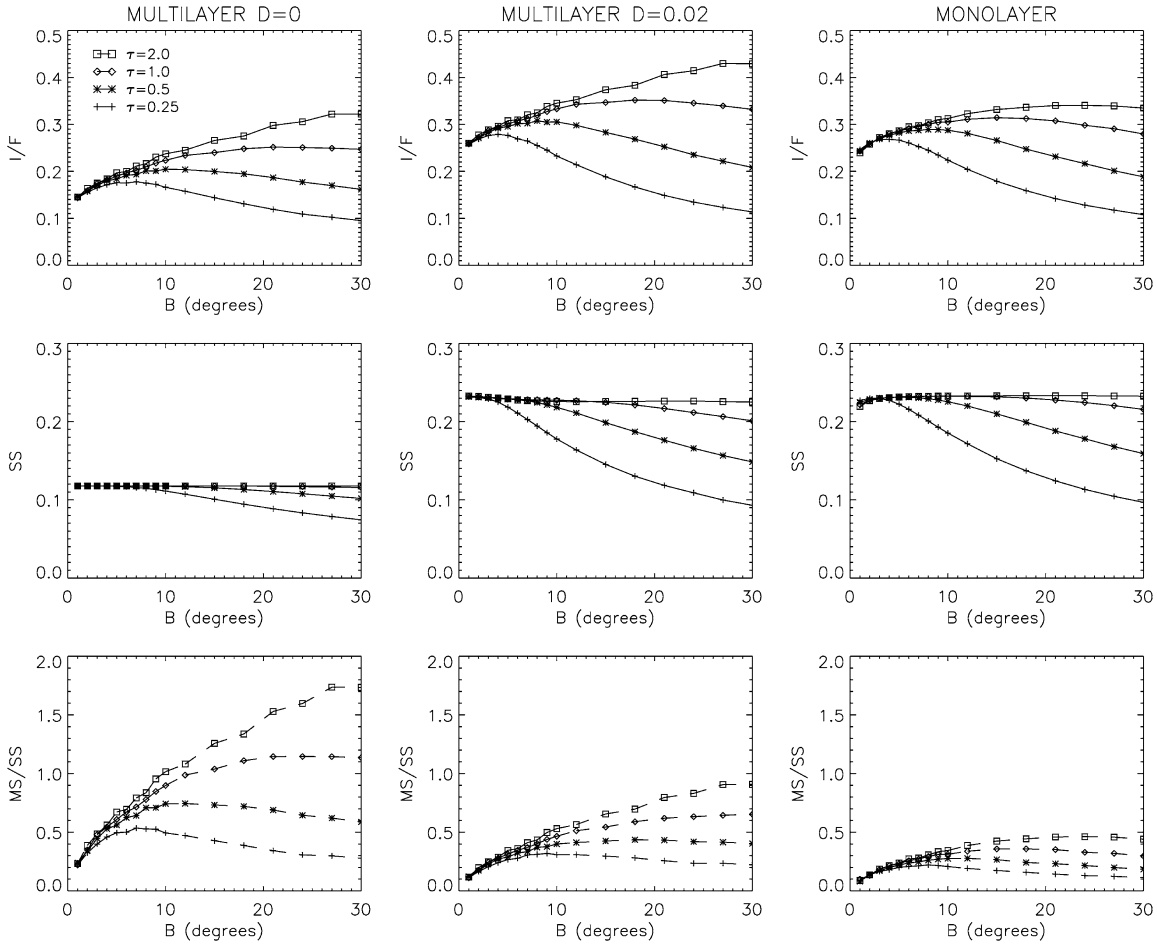

Fig. 16. (Top) Predicted variations in total reflectivity, I/F vs ring opening angle, B at zero phase angle for many-particle-thick and monolayer rings, computed using the irregular particle phase function shown in Fig. 14 for dynamical optical depths of 0.25, 0.5, 1.0, and 2.0. These models have no self-gravity and thus do not exhibit wakes such as those in Fig. 15. The difference between $D = 0$ and $D = 0.02$ multilayer models is that in the former model the numerically calculated single-scattering contribution has been replaced by the analytical formula, Eq. (18), in order to remove the shadow-hiding opposition effect. Shadow hiding is present in the $D = 0.02$ multilayer, as well as in the monolayer model: the single-scattering intensity for the $D = 0.02$ multilayer in fact is very close to Eq. (19). The singly-scattered contributions for the same models are shown separately in the middle panels, while the lower panels show the multiple to single scattering ratios. The latter would be much smaller for a ring composed of backscattering particles.

in the ring will result in stronger wakes. This is illustrated in Fig. 15 by a second model computed with $\tau_{\rm dyn} = 0.8$, for which we find $\beta = 0.20$ at $|B| = 26°$.

Although the models in Fig. 15 were intended primarily to explore the source of the azimuthal asymmetry in the A ring, it may be of some interest to compare their predicted reflectivities and multiple scattering ratios with the radar albedos and polarization ratios. As shown in the second panel in Fig. 15, the simulation with the semi-empirical phase function does quite a good job of reproducing the variation of I/F with B shown by the combined radar data set, though not the very steep decrease in albedo seen in 1999–2003. Contrary to the thick-ring models of Cuzzi and Pollack (1978), and despite a substantial fraction of multiply-scattered flux for $g > 0$, all models in Fig. 15 show a modest decline in reflectivity with increasing tilt angle. This is apparently due to the increasing visibility of the gaps between wakes as the opening angle increases, which also leads to these models' relatively low values of photometric optical depth, $\tau_{\rm phot} = 0.2$–0.4, as shown in the fourth panel.[14] Since the rarefied gaps and wakes are also responsible for the high asymmetry amplitude of the models, it seems that the decline of reflectivity with B is always accompanied by a substantial asymmetry amplitude (see also Salo and Karjalainen, 2003). For the B ring similar models suggest a much smaller β, and a correspondingly weaker decline of reflectivity. Since A and B rings make comparable contributions to the total observed cross-section, the overall decline suggested by the photometric models is even weaker than that seen in Fig. 15.

The Monte Carlo model does not handle polarization explicitly, and thus cannot predict $\mu_{\rm C}$, but we expect $\mu_{\rm C}$ to increase with the fraction of multiple-scattering, as shown in Fig. 9 above. The large values of f and the substantial increase in f with B required to match the observed values of

[14] $\tau_{\rm phot}(B)$ is defined by setting the fraction of light transmitted through the model ring at incidence angle B equal to $\exp(-\tau_{\rm phot}/\sin B)$.

μ_C were illustrated in this figure for an arbitrarily-chosen value of the single-particle polarization ratio, $\mu^* = 0.30$. From Fig. 15, however, we see that while the MS/SS ratio can be large for isotropic or forward-scattering particles, it is almost independent of B, which implies a similarly constant μ_C for a homogeneous ring, at variance with the observations in Fig. 8. Clearly the very steep increase in MS/SS implied by the observed values of μ_C is not compatible with any of the models in Fig. 15 if the internal depolarization is negligible or constant. If, on the other hand, μ^* is permitted to vary with B, as shown in the lower panel in Fig. 9, then it may be possible to fit the observed trend in μ_C.

The Monte Carlo photometric models of Fig. 15 are all special in the sense that they are based on a single dynamical model with strong wakes and a rather low $\tau_{\rm phot}$. In order to check whether the trends shown here have general significance, Fig. 16 compares the predicted I/F vs B for a wide range of optical depths using our irregular particle phase function. The three models studied are an idealized infinite-thickness multilayer (volume density $D = 0$) with no opposition effect, a finite-thickness multilayer with an opposition effect ($D = 0.02$, corresponding to a geometric thickness of 65 particle radii), and a true monolayer. As expected, in each case the MS/SS ratio increases strongly with optical depth, being also larger for the multilayer than the monolayer models. However, even in the extreme case of an idealized multilayer the increase of MS/SS with B is much too weak to account for the observed behavior of μ_C without some dependence of the intrinsic μ^* on B. On the other hand, the models perhaps cast some light on why the μ_C ratios for A and B rings can be so similar, even though they have very different optical thicknesses. According to Fig. 16, for a fixed B the MS/SS ratio is approximately doubled for $\tau = 2$ in comparison with $\tau = 0.5$. But according to Fig. 9, this amounts to only about a 20% increase in μ_C for $\mu^* \simeq 0.3$, and even less for larger values of μ^*. This is in fair agreement with the μ_C values listed in Table 5 for the individual ring components.

From Fig. 16 we also see that, in the absence of wakes, the predicted variations in I/F with B for forward-scattering particles are remarkably similar for multilayer and monolayer models, contrary to the expectations of Cuzzi and Pollack (1978). Over the range of radar detections in Fig. 8 of $12° < |B| < 27°$, the albedo is predicted to decrease by ~17% for the A ring while remaining fairly constant for the B ring.

In summary, the predicted values of both β and average ring reflectivity, I/F shown in Fig. 15 for a near-monolayer A ring composed of moderately forward-scattering ice particles in collisional and gravitational equilibrium are reasonably consistent with the combined set of radar observations, but a detailed match to β may require either an extended size distribution, a larger dynamical optical depth, or both. The minimal variation in multiple scattering fraction with opening angle exhibited by all the Monte Carlo models seems to be incompatible with the observed variation of μ_C in Fig. 8, unless we admit the possibility of a vertically-inhomogeneous ring in which the effective value of μ^* is a function of viewing angle. Models of idealized multilayer and monolayer rings show very similar variations of radar reflectivity with opening angle, but differ in their multiple to single scattering ratios.

Finally, we note that there are serious limitations to the applicability of the Monte Carlo light-scattering model to microwave observations. Chief among these are its strictly geometric optics approach to the light-scattering problem—which neglects the role of diffraction in 'filling in' the geometric shadows behind individual particles—and its neglect of near-field effects due to the close-packing of meter-size ring particles within a layer perhaps only 10 m thick.

7. Conclusions

We summarize our principal conclusions as follows:

1. Delay–Doppler radar images of Saturn's rings obtained in 1999–2003, at a wavelength of 12.6 cm and ring opening angles of $20.1° \leqslant |B| \leqslant 26.7°$, clearly resolve the A and B rings but show no detectable echo from the C ring or Cassini Division. Model fits indicate that the ratio of A ring to B ring normalized cross-section varies from 0.85 to 0.71 over this range of inclinations, and is essentially the same for OC and SC polarizations. The normalized cross-section of the lower optical depth inner B ring is ~2/3 that of the central and outer B ring, and more similar to that of the A ring.
2. The averaged normalized radar cross-section of the A and B rings, $\hat{\sigma}_T$, has decreased from 1.25 ± 0.31 at $B = -20.1°$ to 0.74 ± 0.19 at $B = -26.7°$, with similar fractional changes observed for the A and B rings. These large variations do not appear to be compatible with classical, many-particle-thick models of the rings, or with monolayer models (cf. Cuzzi and Pollack (1978) and Fig. 16), and also appear to be at odds with previous radar observations of the rings (Ostro et al., 1980).
3. The rings' average circular polarization ratio, $\mu_C = \hat{\sigma}_{SC}/\hat{\sigma}_{OC}$ has increased over the same period from 0.64 ± 0.06 to 0.77 ± 0.06, continuing the trend observed by Ostro et al. (1980) for $12° \leqslant |B| \leqslant 18°$. The observed dependence of μ_C on $\sin B$ appears to be linear between 12° and 26°, and is too steep to be explained by an increase in interparticle scattering alone. An inhomogeneous ring with large, irregular particles concentrated towards the mid-plane and surrounded by a haze of smaller, smoother particles may be capable of accounting for the polarization results, due to its elevation angle dependent scattering properties.
4. Using multiple-ringlet model fits to the radar images, we are able to set conservative (3σ) upper limits on the normalized cross-sections of the C ring and Cassini Division of $\hat{\sigma}_T \leqslant 0.03$ and $\hat{\sigma}_T \leqslant 0.09$, respectively, at $|B| =$

23°–26°, substantially improving on the upper limit on the C ring set by Ostro et al. (1982). These very low cross-sections may reflect a substantially larger fraction of smaller (subcentimeter-size) particles in these regions, compositional differences relative to the icy A and B rings, or a greatly reduced level of multiple-scattering.

5. A strong $m = 2$ azimuthal asymmetry is observed in the radar images, concentrated in the A ring, with an amplitude, $\beta \simeq 0.20$ for $|B| \geqslant 23°$. This asymmetry is approximately twice the amplitude of that seen simultaneously in reflected light at visible wavelengths, but has the same orientation with respect to the observer, leading to the conclusion that, like the latter, it also is attributable to the presence of strong gravitational wakes in this part of the rings.
6. A much smaller azimuthal asymmetry may be present in the B ring, at $\sim 1/4$ of the level seen in the A ring but with a similar orientation. A similar weak asymmetry in the inner B ring has recently been reported by (French et al., in preparation) in HST images.
7. Monte Carlo radiative transfer models, based on dynamical simulations of the rings and geometric optics, suggest that the large amplitude of the radar asymmetry in the A ring may be due to the forward-scattering characteristic of cold, decimeter-to-meter-size, irregular water ice particles, which leads to significant multiple scattering even at zero phase angle, and thus to enhanced contrast between wake and interwake regions. A reasonable fit to the observed asymmetry is obtained for a Henyey–Greenstein single particle phase function with a single-scattering albedo, $\varpi = 1.0$ and anisotropy parameter, $g \simeq +0.25$, or for our irregular particle phase function, provided that the maximum particle size and/or the dynamical optical depth are increased somewhat. Such near-monolayer dynamical models predict a total cross-section which decreases slowly with increasing $|B|$, due to the increasing visibility of the low optical depth 'gaps' between the wakes.
8. Radiative transfer models for idealized multilayer and monolayer rings, using the same irregular particle phase function, predict very similar variations in radar albedo with ring opening angle, contrary to the results of Cuzzi and Pollack (1978) but in agreement with those of Froidevaux (1981).
9. We find no evidence in our data for a reappearance of the Low Doppler Excess reported by Goldstein et al. (1977) in radar spectra of the rings from the early 1970s at opening angles exceeding $\sim 24°$.

Although no simple radiative transfer model has yet been identified which simultaneously fits the observed radar cross-section of the rings, their polarization ratio, and the observed variations with ring opening angle, as well as the unexpectedly large azimuthal asymmetry amplitude, promising results have been obtained using the Monte Carlo radiative transfer model developed by Salo and Karjalainen (2003) combined with a moderately forward-scattering particle phase function. The latter is compatible with calculations for irregular water ice particles with power-law size distributions in the centimeter-to-meter size range. It appears that a dynamical near-monolayer may provide an equally good fit to the observed variations of $\hat{\sigma}_T$ and μ_C with B as does a classical, many-particle-thick ring such has generally been favored by previous investigators (e.g., Cuzzi and Pollack, 1978; Ostro et al., 1980). However, no serious attempt has yet been made to optimize the parameters of such a model, or to include an inhomogeneous distribution of scatterers. Furthermore, the Monte Carlo code was developed to model optical data where $\lambda \ll a$, an assumption which is clearly violated at radar wavelengths.

Future monostatic radar observations at Arecibo could go down to $B = -14.5°$ in 2007 and $-8°$ in 2008, albeit with limited tracking time, and could greatly help to narrow the range of possible ring models. We note that both optical observations and the Monte Carlo models of light scattering by gravitational wakes show that β is likely to reach its maximum value at $|B| = 12°$. Bistatic radar observations between Arecibo and Greenbank could yield total ring cross-sections at even lower opening angles, but probably insufficient SNR for delay–Doppler images. Additional observations of μ_C at 3.5 cm by the Goldstone Solar System radar, especially at lower inclinations, would also be most helpful.

During this same time period, we can also look forward to a wealth of observations of the Saturn system by the Cassini spacecraft, including 3-frequency radio occultations by the rings (at 1.3, 3.5, and 12.6 cm) and high-resolution spatial mapping of the scattered radiation from the planet at 2 cm in two linear polarizations by the Radar experiment.

Acknowledgments

We heartily thank Tony Crespo, Victor Negron, Alice Hine, and Phil Perillat at Arecibo for their invaluable assistance with the observations, and Jon Giorgini for providing accurate Saturn ephemerides. Mark Showalter kindly supplied calculations of the irregular particle phase function. The final version of the paper benefited greatly from detailed comments by the two reviewers. The Arecibo Observatory is part of the National Astronomy and Ionosphere Center operated by Cornell University under a cooperative agreement with the National Science Foundation (NSF) and with support from NASA's Planetary Astronomy program. This work was supported in part by the NASA Planetary Geology and Geophysics programs (PDN, RGF, DBC) and by the National Science Foundation (RGF). H.J.S. acknowledges support from the Academy of Finland.

Appendix A. Modeling radar delay–Doppler images of Saturn's rings

We constructed a variety of models of the radial and azimuthal structure of Saturn's main rings in order to estimate their radar reflectivity. These were reprojected into delay–Doppler images, and the model parameters were adjusted by a least squares procedure to give the best match to the radar delay–Doppler observations. To develop and test our procedures, we used high-resolution Hubble Space Telescope (HST) images of the rings as model radar targets. Contemporaneous Wide Field and Planetary Camera 2 (WFPC2) images taken near zero solar phase angle were available for comparison with each of the radar data sets, obtained as part of a long-term program to observe Saturn's rings over a range of ring opening angles (French et al., 2000, 2003).

In the most general case, this reprojection technique enables us to predict the delay–Doppler brightness corresponding to a model (or actual) ring image of arbitrary complexity. Because of the finite delay–Doppler resolution and SNR of the observations, we usually restricted our attention to more idealized models. In the simplest case, we represented the ring system as a set of three concentric, circular ringlets of uniform reflectivity, demarcated by the boundaries of the classical A, B, and C rings. We projected this ring model from radius and longitude coordinates (r, θ) into the sky plane, using the appropriate ring tilt angle B, and for convenience we adopted an angular resolution of one-third of a Planetary Camera pixel ($\sim 0.015''$), corresponding to a spatial resolution at Saturn of $\sim$100 km. (This is 10–20 times higher than the effective resolution of the delay–Doppler images.) This served as the model target for the radar beam.

The model accounts for the (possibly offset) antenna beam profile by multiplying the sky plane image by a 2-dimensional Gaussian of FWHM $= 2.10'$ at $\lambda = 12.6$ cm for the 2001 and 2003 observations, and $2.56'$ for the 1999 and 2000 campaigns, before the surface of the primary reflector was reset. The Gaussian beam profile was squared to account for both transmit and receive losses. In 1999, we suspected a problem with the telescope pointing on one night which we confirmed by performing separate fits to the positive and negative Doppler halves of the images. These fits showed a 15% difference between the reflectivities of the east and west ansa, which did not reappear in subsequent years.

In 2001, an extensive set of pointing calibrations was undertaken by the Observatory staff, which found an RMS pointing error at S-band of $\sim 10''$, subtending $\sim$60,000 km at Saturn. As an independent check of the pointing, and to determine the effect of possible pointing errors on our model fits, we separately fitted the 2000, 2001, and 2003 delay–Doppler images to a grid of three-ringlet models in which the beam was offset from the nominal pointing in the E–W and N–S directions by up to $\pm 120{,}000$ km. (In practice, the pointing errors for the transmitted and received signals are independent, and are likely to be different from each other, but in these tests, we assumed that they were the same.) The best fitting model for the 2000 data had a pointing offset of 22,000 km E and 27,000 km N relative to Saturn's center, or about $6''$, consistent with the independently determined RMS pointing error for the antenna. For 2001 and 2003, the estimated pointing errors from the fits were $5''$ and $3''$, respectively. In all cases, the ring model parameters differed by much less than our quoted uncertainties for the standard fits, which assumed that there was no pointing error.

Obscuration of the rings by the planet was accounted for by computing a mask given by the projected elliptical shape of the planet at the time of the observations, assuming an equatorial radius of 60,268 km at the 1 bar level and an oblateness of 0.09796 (Lindal et al., 1985). The unobscured projected area of each ring region was also computed from the model for use in calculating the normalized radar cross-sections in Table 4.

The Doppler frequency ν and time delay τ of each pixel in the sky plane image was computed from its radius r and longitude θ as follows. Orbital motion was assumed to be circular, with the mean motion Ω of each pixel in the sky plane model image given to order J_4 in terms of Saturn's gravitational harmonics by (Nicholson and Porco, 1988):

$$\Omega^2 = \frac{GM}{r^3}\left[1 + \frac{3}{2}J_2\left(\frac{R_{\rm eq}}{r}\right)^2 - \frac{15}{8}J_4\left(\frac{R_{\rm eq}}{r}\right)^4\right], \qquad \text{(A.1)}$$

where $GM = 3.7931272 \times 10^7$ km^3 s^{-2}, $R_{\rm eq} = 60{,}330$ km, $J_2 = 1.6297 \times 10^{-2}$, and $J_4 = -9.10 \times 10^{-4}$ (Campbell and Anderson, 1989).

The radial component of the orbital velocity is then

$$v_{\rm rad} = \Omega r \sin\theta \cos B \qquad \text{(A.2)}$$

and the corresponding Doppler shift is

$$\nu = -2\nu_0 v_{\rm rad}/c, \qquad \text{(A.3)}$$

while the delay is simply

$$\tau = -2r\cos\theta\cos B/c, \qquad \text{(A.4)}$$

where θ is ring longitude, measured in a prograde direction from the sub-Earth point, $\nu_0 = 2380$ MHz, and c is the speed of light.

A separate delay–Doppler model image was created for each individual ringlet in the sky plane image, at the same resolution in ν (2000 kHz) and τ (10 ms) as the processed radar images. The contribution of reflecting area from each unobscured pixel in the sky-plane image was added to the appropriate delay–Doppler pixel. To simulate the finite pulse length of the transmitted signal, the delay–Doppler model was convolved in the time domain by a trapezoidal kernel of the appropriate duration (see Table 1). We performed a series of tests to confirm that any errors in registration of the model and observations were less than half a resolution element in ν and τ.

At this stage, the simple concentric ring model had been mapped into (ν, τ) space and was directly comparable to the radar image. Using a non-linear least-squares algorithm, the

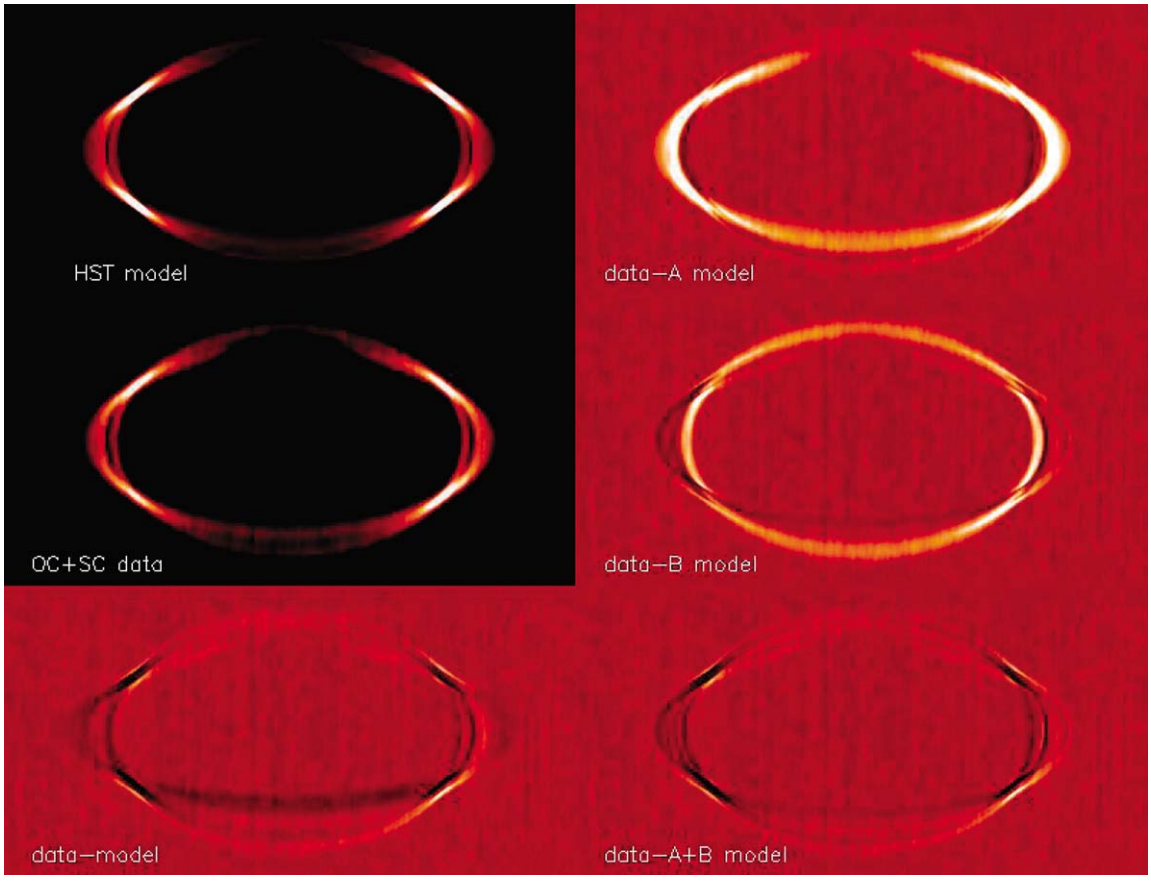

Fig. 17. A synthetic delay–Doppler image derived by reprojecting a pair of overlapping HST Planetary Camera images (upper left), compared with the corresponding radar image constructed from OC and SC data obtained in December 2001 (middle left panel). The HST image has been smoothed in Doppler and delay to match the resolution of the radar image. The upper right panel shows a radar image of the B ring alone, obtained by subtracting a suitably-scaled HST image of the A ring based on a 2-parameter fit. The middle right panel shows a radar image of the A ring, obtained by subtracting a suitably-scaled HST image of the B ring based on the same 2-parameter fit. At lower left is shown the residual image after subtracting the entire HST model, scaled on the basis of a 1-parameter fit, from the radar image. Note the negative residuals in the regions dominated by the C ring. The lower right panel shows the residual image after subtracting best-fitting individually-scaled A and B ring images.

individual ringlet 'reflectivities' were then adjusted so that the composite model delay–Doppler image, obtained by co-adding the individual ringlet images, gave the best match to the data. The mean background signal was assumed to be zero, rather than being fitted, because the preprocessing of the radar data described in Section 3 produced a zero background to high precision. In practice, the delay–Doppler images for the ringlet models were computed in advance and stored on disk. With this computationally intensive task behind us, a series of fits to the OC, SC, and combined CBR and PFS datasets could be performed quite quickly.

We tested the algorithm extensively. In one test, we formed a composite image of Saturn's rings from separate WFPC2 images of the E and W ansae, mapped the observed ring brightness into (ν, τ) space as described above, and fitted this simulated radar image using a model with eight uniform ringlets. We then compared the relative reflectivities for the model ringlets with the actual radial reflectivity profile of the rings extracted from the HST data. The agreement was excellent.

As an illustration of the ability of the model to distinguish the separate reflectivities of the A and B rings, in spite of the degeneracy in the delay–Doppler image, Fig. 17 shows the combined OC + SC radar image obtained in December 2001, together with a delay–Doppler image constructed from HST data taken at the same ring opening angle. The reflectivities of the A and B rings in the HST image were then separately scaled to give the best match to the radar data. By subtracting the A ring model from the data, the radar signal from the B ring remains, and vice versa. Note that the four brightness peaks in the images due to the delay–Doppler mapping degeneracy are still present in the individual rings, but much subdued in comparison with the original radar image where the A and B rings appear to cross over in these regions (cf. discussion of Fig. 1 above). The final panel in Fig. 17 shows the residuals after subtracting both A and B ring models from the data.

To estimate the azimuthal asymmetry in the rings' radar brightness, we included additional components in the ringlet model based on Monte Carlo light scattering calculations for

N-body representations of gravitational wakes. In principle, one could generalize the models described above by including, for any desired radial ring region, separate sine and cosine Fourier components of a periodic azimuthal brightness variation with wavenumber $m = 1, 2, 3 \ldots$, and fit for their amplitudes and phases. But the lower delay resolution of the images compared with their Doppler resolution, which introduces a radial resolution which is longitude-dependent, and the strong concentrations of radar brightness due to the delay–Doppler degeneracy in the vicinity of the predicted brightness minima argue against such an unconstrained ab initio approach to measuring the brightness asymmetry.

We have instead chosen to model the asymmetry using previous N-body simulations of particle wakes by Salo (1995) and Salo et al. (2004). These simulations employed a local patch model with periodic boundary conditions and colliding, self-gravitating particles. All calculations are based on the same dynamical realization of the rings, as described by Salo et al. (2004) and illustrated in their Fig. 2, using ∼5000 identical particles of radius 1.67 m and density 0.45 g cm^{-3}, a ring radius of 130×10^3 km, a dynamical optical depth of 0.5 (appropriate to the middle A ring) and the coefficient of restitution measured for cold ice by Bridges et al. (1984). The size of the simulation region corresponds to $4\lambda_{cr} \times 4\lambda_{cr}$, where λ_{cr} is the critical wavelength from Eq. (21) above; this should represent a sufficiently large region to give approximately correct orientations and amplitudes of the wakes.

The azimuthal variation in ring brightness was computed at zero phase angle and for values of $|B|$ appropriate to the HST and radar observations, using a Monte Carlo ray tracing scheme based on geometric optics and incorporating multiple-scattering (see Salo and Karjalainen (2003) for a complete description). This radiative transfer code uses 30,000 photons at each longitude and the results are averaged over 40 snapshots from the dynamical simulation. In the models fitted to the Voyager and HST data (Salo et al., 2004; French et al., in preparation), either a Lambert sphere phase function or a power-law phase function approximating that of Callisto (see Dones et al., 1993) was used, with a single scattering albedo $\varpi \simeq 0.5$. In our fits to the radar data we assumed for simplicity a 'reference model' employing a Lambert sphere phase function with $\varpi = 1.0$, but permitted the amplitude of the model asymmetry to vary in order to achieve the best fit.

As a test of our implementation of the asymmetry model, we fitted the projected HST delay–Doppler image in Fig. 17 to a 3-ringlet model with an A-ring asymmetry, and found good agreement with direct azimuthal scans of the HST data. We are thus confident that the large asymmetry amplitudes found for the radar images in Section 5.2, as compared with those seen in contemporaneous HST images, are real and not artifacts due to any geometric peculiarities intrinsic to delay–Doppler images of the rings.

References

Berge, G.L., Muhleman, D.O., 1973. High-angular observations of Saturn at 21.1-centimeter wavelength. Astrophys. J. 185, 373–382.

Black, G.J., Campbell, D.B., Nicholson, P.D., 2001. Icy Galilean satellites: Modeling radar reflectivities as a coherent backscatter effect. Icarus 151, 167–180.

Bridges, F.G., Hatzes, A., Lin, D.N.C., 1984. Structure, stability and evolution of Saturn's rings. Nature 309, 333–335.

Camichel, H., 1958. Mesures photométriques de Saturne et de son anneau. Ann. d'Astrophys. 21, 231–242.

Campbell, J.K., Anderson, J.D., 1989. Gravity field of the saturnian system from Pioneer and Voyager tracking data. Astron. J. 97, 1485–1495.

Campbell, D.B., Chandler, J.F., Ostro, S.J., Pettengill, G.H., Shapiro, I.I., 1978. Galilean satellites—1976 radar results. Icarus 34, 254–267.

Campbell, D.B., Hudson, R.S., Margot, J-L., 2002. Advances in Planetary Radar Astronomy. In: Stone, W.R. (Ed.), Review of Radio Science 1999–2002. IEEE Press/Wiley–Interscience, New York, pp. 866–869.

Chandrasekhar, S., 1960. Radiative Transfer. Dover, New York.

Colombo, G., Goldreich, P., Harris, A.W., 1976. Spiral structure as an explanation for the asymmetric brightness of Saturn's A ring. Nature 264, 344–345.

Cooke, M.L., 1991. Saturn's rings: Photometric studies of the C ring and radial variation in the Keeler gap. Ph.D. thesis, Cornell University.

Cuzzi, J.N., Estrada, P.R., 1998. Compositional evolution of Saturn's rings due to meteoroid bombardment. Icarus 132, 1–35.

Cuzzi, J.N., Pollack, J.B., 1978. Saturn's rings—particle composition and size distribution as constrained by microwave observations. I. Radar observations. Icarus 33, 233–262.

Cuzzi, J.N., Burns, J.A., Durisen, R.H., Hamill, P.M., 1979. The vertical structure and thickness of Saturn's rings. Nature 281, 202–204.

Cuzzi, J.N., Pollack, J.B., Summers, A.L., 1980. Saturn's rings—particle composition and size distribution as constrained by observations at microwave wavelengths. II. Radio interferometric observations. Icarus 44, 683–705.

Cuzzi, J.N., Lissauer, J.J., Esposito, L.W., Holberg, J.B., Marouf, E.A., Tyler, G.L., Boischot, A., 1984. Saturn's rings: Properties and processes. In: Greenberg, R., Brahic, A. (Eds.), Planetary Rings. Univ. of Arizona Press, Tucson, pp. 73–199.

Daisaka, H., Ida, S., 1999. Spatial structure and coherent motion in dense planetary rings induced by self-gravitational instability. Earth Planets Space 51, 1195–1213.

de Pater, I., Dickel, J.R., 1991. Multifrequency radio observations of Saturn at ring inclination angles between 5 and 26 degrees. Icarus 94, 474–492.

Dones, L., Cuzzi, J.N., Showalter, M.R., 1993. Voyager photometry of Saturn's A ring. Icarus 105, 184–215.

Doyle, L.R., Dones, L., Cuzzi, J.N., 1989. Radiative transfer modeling of Saturn's outer B ring. Icarus 80, 104–135.

Dunn, D.E., Molnar, L.A., Fix, J.D., 2002. More microwave observations of Saturn: Modeling the ring with a Monte Carlo radiative transfer code. Icarus 160, 132–160.

Dunn, D.E., Molnar, L.A., Niehof, J.T., de Pater, I., Lissauer, J.J., 2004. Microwave observations of Saturn's rings: Anisotropy in directly transmitted light. Icarus 171, 183–198.

Esposito, L.W., O'Callaghan, M., Simmons, K.E., Hord, C.W., West, R.A., Lane, A.L., Pomphrey, R.B., Coffeen, D.L., Sato, M., 1983a. Voyager photopolarimeter stellar occultation of Saturn's rings. J. Geophys. Res. 88, 8643–8649.

Esposito, L.W., O'Callaghan, M., West, R.A., 1983b. The structure of Saturn's rings—implications from the Voyager stellar occultation. Icarus 56, 439–452.

Estrada, P.R., Cuzzi, J.N., 1996. Voyager observations of the color of Saturn's rings. Icarus 122, 251–272.

Evans, J.V., Hagfors, T., 1968. Radar Astronomy. McGraw–Hill, New York.

Franklin, F.A., Colombo, G., 1978. On the azimuthal brightness variations of Saturn's rings. Icarus 33, 279–287.

French, R.G., Nicholson, P.D., 2000. Saturn's rings. II. Particle sizes inferred from stellar occultation data. Icarus 145, 502–523.
French, R.G., Dones, L., Salo, H., 2000. HST observations of the azimuthal brightness asymmetry in Saturn's rings. Bull. Am. Astron. Soc. 32, 864.
French, R.G., McGhee, C.A., Dones, L., Lissauer, J.J., 2003. Saturn's wayward shepherds: The peregrinations of Prometheus and Pandora. Icarus 162, 143–170.
Froidevaux, L., 1981. Saturn's rings—infrared brightness variation with solar elevation. Icarus 46, 4–17.
Gehrels, T., Esposito, L.W., 1981. Pioneer fly-by of Saturn and its rings. Adv. Space Res. 1, 67–71.
Goldstein, R.M., Morris, G.A., 1973. Radar observations of the rings of Saturn. Icarus 20, 249–283.
Goldreich, P., Tremaine, S.D., 1978. The velocity dispersion in Saturn's rings. Icarus 34, 227–239.
Goldstein, R.M., Green, R.R., Pettengill, G.H., Campbell, D.B., 1977. The rings of Saturn—two-frequency radar observations. Icarus 30, 104–110.
Grossman, A.W., Muhleman, D.O., Berge, G.L., 1989. High-resolution microwave images of Saturn. Science 245, 1211–1215.
Hämeen-Anttila, K.A., Vaaraniemi, P., 1975. A theoretical photometric function of Saturn's rings. Icarus 25, 470–478.
Hapke, B., 1986. Bidirectional reflectance spectroscopy. IV. The extinction coefficient and the opposition effect. Icarus 67, 264–280.
Hapke, B., 1990. Coherent backscatter and the radar characteristics of outer planet satellites. Icarus 88, 407–417.
Harmon, J.K., Perillat, P.J., Slade, M.A., 2001. High-resolution radar imaging of Mercury's north pole. Icarus 149, 1–15.
Irvine, W.M., 1966. The shadowing effect in diffuse reflection. J. Geophys. Res. 71, 2931–2937.
Julian, W.H., Toomre, A., 1966. Non-axisymmetric responses of differentially rotating disks of stars. Astrophys. J. 146, 810–830.
Lane, A.L., Hord, C.W., West, R.A., Esposito, L.W., Coffeen, D.L., Sato, M., Simmons, K.E., Pomphrey, R.B., Morris, R.B., 1982. Photopolarimetry from Voyager 2—preliminary results on Saturn, Titan, and the rings. Science 215, 537–543.
Lindal, G.F., Sweetnam, D.N., Eshleman, V.R., 1985. The atmosphere of Saturn—an analysis of the Voyager radio occultation measurements. Astron. J. 90, 1136–1146.
Lumme, K., Irvine, W.M., 1984. Azimuthal variations in Saturn's A ring. In: IAU Colloq. 75: Planetary Rings, pp. 87–91.
Marouf, E.A., Tyler, G.L., Zebker, H.A., Simpson, R.A., Eshleman, V.R., 1983. Particle size distributions in Saturn's rings from Voyager 1 radio occultation. Icarus 54, 189–211.
Molnar, L.A., Dunn, D.E., Niehof, J.T., 1999. Fall 1998 radio observations of Saturn's rings: New evidence of ring wakes. Bull. Am. Astron. Soc. 31, 1141.
Nicholson, P.D., Porco, C.C., 1988. A new constraint on Saturn's zonal gravity harmonics from Voyager observations of an eccentric ringlet. J. Geophys. Res. 93, 10209–10224.
Nicholson, P.D., Showalter, M.R., Dones, L., French, R.G., Larson, S.M., Lissauer, J.J., McGhee, C.A., Sicardy, B., Seitzer, P., Danielson, G.E., 1996. Observations of Saturn's ring-plane crossing in August and November. Science 272, 509–516.
Nicholson, P.D., French, R.G., Tollestrup, E., Cuzzi, J.N., Harrington, J., Matthews, K., Perkovic, O., Stover, R.J., 2000. Saturn's rings. I. Optical depth profiles from the 28 Sgr occultation. Icarus 145, 474–501.
Ostro, S.J., 1993. Planetary radar astronomy. Rev. Mod. Phys. 65, 1235–1279.
Ostro, S.J., Pettengill, G.H., 1984. A review of radar observations of Saturn's rings. In: IAU Colloq. 75: Planetary Rings, pp. 49–55.
Ostro, S.J., Pettengill, G.H., Campbell, D.B., 1980. Radar observations of Saturn's rings at intermediate tilt angles. Icarus 41, 381–388.
Ostro, S.J., Pettengill, G.H., Campbell, D.B., Goldstein, R.M., 1982. Delay–Doppler observations of Saturn's rings. Icarus 49, 367–381.
Ostro, S.J., Campbell, D.B., Simpson, R.A., Hudson, R.S., Chandler, J.F., Rosema, K.D., Shapiro, I.I., Standish, E.M., Winkler, R., Yeomans, D.K., 1992. Europa, Ganymede, and Callisto—new radar results from Arecibo and Goldstone. J. Geophys. Res. 97, 18227–18244.
Pettengill, G.H., Hagfors, T., 1974. Comment on radar scattering from Saturn's rings. Icarus 21, 188.
Pollack, J.B., 1975. The rings of Saturn. Space Sci. Rev. 18, 3–93.
Pollack, J.B., Summers, A., Baldwin, B., 1973. Estimates of the sizes of the particles in the rings of Saturn and their cosmogonic implications. Icarus 20, 263–278.
Poulet, F., Sicardy, B., Dumas, C., Jorda, L., Tiphène, D., 2000. The crossings of Saturn ring plane by the Earth in 1995: Ring thickness. Icarus 145, 147–165.
Poulet, F., Cruikshank, D.P., Cuzzi, J.N., Roush, T.L., French, R.G., 2003. Compositions of Saturn's rings A, B, and C from high resolution near-infrared spectroscopic observations. Astron. Astrophys. 412, 305–316.
Reitsema, H.J., Beebe, R.F., Smith, B.A., 1976. Azimuthal brightness variations in Saturn's rings. Astron. J. 81, 209–215.
Salo, H., 1992a. Gravitational wakes in Saturn's rings. Nature 359, 619–621.
Salo, H., 1992b. Numerical simulations of dense collisional systems. II. Extended distribution of particle sizes. Icarus 96, 85–106.
Salo, H., 1995. Simulations of dense planetary rings. III. Self-gravitating identical particles. Icarus 117, 287–312.
Salo, H., Karjalainen, R., 1999. Dynamical and photometric modeling of azimuthal brightness asymmetry in Saturn's rings. Bull. Am. Astron. Soc. 31, 1160.
Salo, H., Karjalainen, R., 2003. Photometric modeling of Saturn's rings. I. Monte Carlo method and the effect of non-zero volume filling factor. Icarus 164, 428–460.
Salo, H., Karjalainen, R., French, R.G., 2004. Photometric modeling of Saturn's rings. II. Azimuthal asymmetry in reflected and transmitted light. Icarus 170, 70–90.
Showalter, M.R., Cuzzi, J.N., 1993. Seeing ghosts—photometry of Saturn's G ring. Icarus 103, 124–143.
Showalter, M.R., Nicholson, P.D., 1990. Saturn's rings through a microscope: Particle size constraints from the Voyager PPS scan. Icarus 87, 285–306.
Showalter, M.R., Pollack, J.B., Ockert, M.E., Doyle, L.R., Dalton, J.B., 1992. A photometric study of Saturn's F ring. Icarus 100, 394–411.
Sicardy, B., Lecacheux, J., Laques, P., Despiau, R., Auge, A., 1982. Apparent thickness and scattering properties of Saturn's rings from March 1980 observations. Astron. Astrophys. 108, 296–305.
Thompson, W.T., Lumme, K., Irvine, W.M., Baum, W.A., Esposito, L.W., 1981. Saturn's rings—azimuthal variations, phase curves, and radial profiles in four colors. Icarus 46, 187–200.
Toomre, A., 1964. On the gravitational stability of a disk of stars. Astrophys. J. 139, 1217–1238.
Toomre, A., Kalnajs, A.J., 1991. Spiral chaos in an orbiting patch. In: Sundelius, B. (Ed.), Dynamics of Disc Galaxies. Almquist & Wiksell, Stockholm, pp. 341–358.
Tyler, G.L., Marouf, E.A., Simpson, R.A., Zebker, H.A., Eshleman, V.R., 1983. The microwave opacity of Saturn's rings at wavelengths of 3.6 and 13 cm from Voyager 1 radio occultation. Icarus 54, 160–188.
Van der Tak, F., de Pater, I., Silva, A., Millan, R., 1999. Time variability in the radio brightness distribution of Saturn. Icarus 142, 125–147.
Zebker, H.A., Tyler, G.L., 1984. Thickness of Saturn's rings inferred from Voyager 1 observations of microwave scatter. Science 223, 396–398.
Zebker, H.A., Marouf, E.A., Tyler, G.L., 1985. Saturn's rings—particle size distributions for thin layer models. Icarus 64, 531–548.